Applied Research

Applied Research

RESEARCH ARTICLE OPEN ACCESS

Scaling Up of a Lightweight Aggregates System Based on Recovery Raw Materials and With Fertilisation Capacity: From Laboratory Prototype to Semi-Industrial Production

Martina Napolitano[1] | Giulia Malvolti[1] | Fernanda Andreola[1] | Isabella Lancellotti[1] | Gianluca Malavasi[2] | Michelina Catauro[3] | Antonio D'Angelo[3] | Luisa Barbieri[1,4]

[1]Department of Engineering "Enzo Ferrari", University of Modena and Reggio Emilia, Modena, Italy | [2]Department of Chemical and Geological Sciences, University of Modena and Reggio Emilia, Modena, Italy | [3]Department of Engineering, University of Campania "Luigi Vanvitelli", Aversa, Italy | [4]Interdepartmental Research Center for the Improvement and Valorisation of Agro-Food Biological Resources of the University of Modena and Reggio Emilia Biogest-Siteia, Reggio Emilia, Italy

Correspondence: Luisa Barbieri (luisa.barbieri@unimore.it)

Received: 3 February 2026 | **Revised:** 22 June 2026 | **Accepted:** 7 August 2026

Funding: European Commission

Keywords: clay-based aggregates | glass fertiliser | nutrient recovery | slow-release fertiliser | technology readiness levels

ABSTRACT

This study evaluates the semi-industrial prototyping of a sustainable phosphorus-potassium (PK) fertiliser (ABVF) developed at laboratory scale, using red clay and waste-derived materials as biochar, spent coffee grounds, and cullet glass. A new fertiliser glass composition was developed to ensure industrial meltability, while enabling low-temperature processing. Micropellets were manufactured through semi-industrial cold extrusion and firing, yielding mechanically stable aggregates with controlled porosity. Chemical and physical characterisation showed that firing enhances structural integrity, porosity distribution, favouring water retention and gradual nutrient diffusion. Chemical analyses confirmed enrichment of P_2O_5 and K_2O in fired aggregates, with leaching tests demonstrating a more sustained release of P and K in citric acid compared to raw aggregates, and high resistance to leaching under acetic acid conditions, indicating potential to minimise nutrient losses in field applications. Antimicrobial assays revealed that both raw and fired aggregates inhibited bacterial growth, suggesting additional benefits for storage stability. A 6-month field trial on turfgrass and photinia shrubs demonstrated that fired ABVF can match the performance of a conventional NPK fertiliser. By integrating materials processing, nutrient release control, and agronomic validation, this work demonstrates the feasibility of producing sustainable PK fertilisers at semi-industrial scale from recovered resources.

1 | Introduction

Phosphorus (P) and potassium (K) are two of the three primary macronutrients essential for plant growth, alongside nitrogen. Phosphorus is a vital component of adenosine triphosphate (ATP), nucleic acids, and phospholipids, playing central roles in energy transfer, photosynthesis, cell division, and genetic information processing. Adequate phosphorus availability supports robust root development, enhances flowering and seed formation, and improves overall crop quality [1–3]. Potassium is indispensable in physiological regulation, facilitating the movement of water,

Abbreviations: AA, acetic acid; BET, Brunauer-Emmett-Teller; CA, citric acid; CFU, colony forming units; EC, electrical conductivity; HSM, heating stage microscopy; L.O.I., loss on ignition; MIP, mercury intrusion porosimetry; NPK, nitrogen-phosphorus-potassium; PK, phosphorus-potassium; PPD, petri plate diameter; SCGs, spent coffee grounds; SEM, scanning electron microscopy; WDXRF, wavelength dispersive X-ray fluorescence; XRF, X-ray fluorescence.

nutrients, and carbohydrates within plant tissues, and activates numerous enzymes involved in protein synthesis and metabolism [4, 5]. Deficiencies in either P or K result in stunted growth, reduced yield, and diminished crop quality, highlighting their indispensable roles in plant productivity and resilience. Modern agriculture relies heavily on mineral-based P and K fertilisers to maintain crop yields. However, these fertilisers are derived from non-renewable mineral reserves: phosphate rock for phosphorus and potash ore for potassium. Phosphate rock reserves are being depleted at an unsustainable rate, raising long-term concerns for food security [6, 7]. This geologic scarcity is compounded by geopolitical constraints, since rich phosphate deposits are highly localised [8]. Potassium salts are similarly limited and also face supply risks due to geographic concentration [9], making global food systems vulnerable to price volatility and supply shocks.

Moreover, the production of conventional P and K fertilisers imposes significant environmental burdens. Phosphorus is typically extracted by mining phosphate rock and processing it with sulfuric acid to produce soluble forms such as superphosphates. This process generates large volumes of hazardous waste, including phosphogypsum, which contains toxic heavy metals (like cadmium) and radioactive elements [10–12]. Furthermore, the phosphate industry emits pollutants such as sulfur dioxide and fluoride gases, contributing to air and soil contamination [13]. Potash fertilisers, primarily potassium chloride, are mined from evaporite deposits. These operations generate salt tailings that, without proper management, lead to leaching of chloride and sodium into nearby water bodies. In regions where potash is heavily mined, river salinity levels have risen dramatically, with documented ecological damage to freshwater systems [14–16].

Once applied to fields, conventional P and K fertilisers often exhibit low nutrient use efficiency (NUE). Soluble phosphate fertilisers are highly prone to runoff; phosphorus can be washed away by rainfall before plants absorb it, leading to eutrophication, nutrient over-enrichment of water bodies that fuels algal blooms, depletes oxygen, and harms aquatic life [17]. Applied phosphorus rapidly binds with soil minerals (such as iron, aluminum, calcium), becoming immobilised in forms unavailable to plants. Consequently, crop uptake of P is often less than 20% in the season of application [18].

While potassium is generally more stable in soil due to its cationic nature and affinity for soil exchange sites, inefficiencies still occur. In sandy soils with low cation exchange capacity, potassium can leach beyond root zones [19]. In contrast, certain clay soils can fix potassium between mineral layers, rendering it temporarily unavailable to plants [20]. Overapplication of potassium, especially potassium chloride, can also contribute to water and soil salinization.

To address the inefficiencies and environmental burdens associated with conventional fertilisers, there is growing interest in slow-release fertilisers (SRFs). These formulations aim to synchronise nutrient release with plant uptake, reducing losses and enhancing nutrient efficiency. While SRFs have historically focused on nitrogen, emerging research is developing slow-release formulations for phosphorus and potassium [21–27]. Interest is also demonstrated by the expanding global market for SRFs, thanks to the agricultural and environmental benefits associated: capacity to improve the efficiency of crop production per hectare, flexibility in application, equal distribution of nutrients to crops, reduction of toxicity, especially for seedlings, because the use of conventional fertilisers has a high ion concentration, which induces osmotic stress and causes damage at different growth stages.

A complementary strategy is nutrient recycling, recovering P and K from organic and industrial waste streams and converting them into fertilisers. This aligns with circular economic principles and reduces dependence on virgin mineral resources. Struvite is a prime example: it can be precipitated by municipal or industrial wastewater, providing a slow-release source of phosphorus while preventing nutrient pollution [28]. Struvite's low water solubility minimises runoff losses and supports sustained crop uptake. In waste streams lacking ammonium but rich in potassium, potassium struvite ($MgKPO_4{\cdot}6H_2O$) can be recovered and used as a dual-source fertiliser supplying both P and K [29].

Other materials, such as bone char (from thermally treated animal bones), are also promising. Bone char contains stable calcium phosphate, acting as a slow-release P source with reduced leaching potential [30, 31]. Additionally, ash from biomass (crop residues, poultry litter, wood combustion) often contains potassium and phosphorus [32, 33], which can be processed into plant-available forms. Biochar, produced via pyrolysis of organic matter, is another promising carrier for recycled nutrients. When derived from P- and K-rich biomass, biochar can serve as a nutrient-retentive soil amendment, releasing nutrients slowly and improving soil structure and microbial activity [34, 35].

Increasing regulatory support, such as inclusion of recycled materials in the EU Fertilising Products Regulation, evolving EU nutrient policies shifting from pollution control toward circular economy objectives [36], is creating stronger incentives for recycled fertilisers.

Meanwhile, investments in scaling technologies are accelerating their path toward mainstream adoption. The industrial production of fertilisers in pellets or granules generally involves several key steps, each governed by specific parameters to ensure product quality. Initially, raw materials are blended in defined proportions to obtain a homogeneous mixture, while maintaining moisture content typically between 10 and 20 wt%, depending on the raw material characteristics. This is followed by pelletizing, where the mixture is extruded through specialised matrices to form pellets. Subsequent steps include cooling to stabilise pellet structure, screening to separate pellets meeting size specifications, drying, and finally sintering (induration) to consolidate the material. For clay-based pellets or aggregates, firing is typically performed in rotary kilns at high temperatures (in a range 1100°C–1300°C) [37]. Previous studies by the authors demonstrated that fired aggregates with suitable mechanical and physical properties could be achieved using a static furnace at significantly lower temperatures (around 1000°C), offering potential energy savings compared to conventional industrial processes [38].

This study explores the product/process functional testing of using waste-derived materials, specifically biochar, spent coffee grounds (SCGs), bone ash, pumice residues, and recycled glass, as precursors for PK SRFs, starting from the good agronomic performances tested previously by the authors in the form of a new SRF system for Nursery Grapevine [39]. Each component was selected for its functional contribution to the final aggregate. Clay offers excellent processability and, when fired, produces low-density yet high-strength granules suitable for multiple applications in agriculture, horticulture, and green infrastructure [40]. Biochar has been reported to enhance water-holding capacity and reduce bulk density in substrate systems, such as those used in green roofs, thereby improving nutrient retention and minimising leaching [41]. After firing, biochar can further increase the aggregate's surface area and porosity, improving nutrient release dynamics. Similarly, SCGs, with its high organic matter content, acts as an effective pore-forming agent during thermal processing. The nutrient properties of the aggregates were further enhanced by incorporating a specifically engineered fertilising glass, optimised in this study to improve nutrient release while ensuring compatibility with industrial meltability requirements. Starting from an Italian patent of the authors of 2020 (Italian Patent for industrial invention n.102018000009844, 09.30.2020 [42]), where a clay-based SRF (ABVF) was developed at laboratory scale (TRL 3–4), this study aims to verify industrial transferability through the transition phase of semi-industrial prototyping with the aim of verifying that the process works in conditions close to industrial reality (TRL 5–6) and assess the resulting products in terms of both technical and agronomic performance. To this purpose, micropellets were produced using semi-industrial equipment and evaluated based on their chemical, physical, and antimicrobial properties. Two product variants, before and after firing, were characterised for physical and chemical properties, nutrient composition, and release kinetics under acidic conditions simulating rhizospheric activity and environmental leaching scenarios. Preliminary greenhouse trials on lettuce were conducted to verify the absence of phytotoxicity and to evaluate short-term plant responses. Based on these results, the most promising formulation was selected for a 6-month field trial on *Photinia fraseri* (photinia) and turfgrass (*Festuca arundinacea* and *Poa pratensis*).

Recent studies have explored several components relevant to the present work, including biochar-based SRFs, clay-containing nutrient carriers, and multicomponent glass fertilisers. Biochar-based fertilisers have been widely investigated as nutrient carriers and soil amendments, although their performance depends strongly on activation, formulation strategy, nutrient loading, and soil conditions [34, 43]. Hydrotalcite, starch, and biochar-based composite fertilisers, for example, have been proposed to improve water retention and reduce N, P, and K leaching, but they are generally developed as biochar-centred carrier systems [44]. Clay-containing fertiliser systems have also been studied as nutrient-release modulators, where natural or modified clays act as carriers or co-granulation additives to tune fertiliser dissolution [45]. Similarly, recent glass-fertiliser studies have demonstrated that multicomponent silicate-phosphate glasses can be compositionally designed to release P, K, and micronutrients through pH-dependent glass dissolution [46, 47]. SCGs and their derivatives have also been reviewed as promising soil amendments, as well as interesting materials to improve nutrient availability in liquid NPK fertilisers, or carrier for biofertilisers, although direct use may be limited by phytotoxicity or N immobilisation unless they are stabilised or thermally processed [48]. Even closer to the present topic, a study recently evaluated phosphate glass and biochar as sustainable fertilising materials for rose plantings, confirming the agronomic interest of combining a glass-based nutrient source with a carbonaceous soil amendment [49]. However, the two components were tested as powder soil amendments, whereas the present work integrates the glassy PK source, clay matrix, biochar, and SCGs into a single extruded and fired aggregate. Therefore, the novelty of the present work does not reside in the isolated use of clay, biochar, SCGs, or glass-derived fertilisers, but in the integration of these components into a single waste-derived PK aggregate, in which the clay phase provides extrusion and firing processability, biochar and SCGs contribute to porosity and matrix functionality, and the engineered glass frit acts as the main P and K reservoir.

2 | Materials and Methods

2.1 | Materials

The fertiliser system developed in this study (called ABVF) was formulated by blending four components: red clay, biochar, SCGs, and a specially engineered glass-based fertiliser. The primary constituent, a local red ferruginous clay, was sourced from the Samone quarry in the municipality of Zocca (MO). SCGs are derived from the extraction of raw coffee powder with hot water or steam for beverage preparation. SCGs typically exhibit a high moisture content (approximately 65 wt%); therefore, they were air-dried at room temperature for 2 days, reducing the moisture level to around 7 wt%, a threshold sufficient to minimise the risk of mold and fungal growth.

The biochar utilised was an Italian product (Gruppo RM Energy Solutions), derived as a by-product of the pyrolysis of exhausted chestnut wood following steam-current treatment for extracting a distillate, a plant-based extract rich in organic compounds.

The glassy fertiliser component was designed by researchers at the Ceramic Laboratory, Department of Engineering "Enzo Ferrari," using recovered raw materials including glassy sand obtained as an end-of-waste (EoW) material from processed packaging glass cullet, animal bone meal ash, pumice scraps from quarrying operations, and adding industrial grade potassium carbonate. The glass formulation was optimised to meet the minimum P_2O_5 and K_2O content corresponding to 12 wt% required for glass matrix fertilisers, in compliance with Italian Regulation D.Lgs. 75/2010, All 1.

Other materials used for chemical tests include Citric acid (≥ 99.5%, ACS grade), Acetic acid (100%, Suprapur), Nitric Acid (65%, Suprapur), Sulfuric Acid (96%, Ultrapur), Sodium Hydroxide (≥ 99%, ACS grade), Sodium molybdate dihydrate (≥ 99.5%), Ammonium molybdate (99.98% trace metals basis), Quinoline (reagent grade, 98%) and dipotassium phosphate (ACS reagent, ≥ 98%), by Sigma-Aldrich. Kjeldahl Selenium Catalyst Tablets, Technical, were acquired from Fisher Chemical.

2.2 | Glass Realisation

The glassy fertiliser component was designed starting from an initial formulation containing the above cited raw materials (except for pumice scraps) whose details on chemical analysis and application are reported in a previous paper by the authors [38]. The expansion carried out in this study involved the realisation of a series of formulations until the one offering the best processing performance was selected. The same quantitative ratios of nutrient carriers (P and K from animal bone meal ash and K_2CO_3) and of vitrifying agent were maintained, but in the latter case the mineral residue was also included. To be more precise, five formulations were prepared by varying the pumice-to-glass cullet ratio, within 40 parts of melting component. This modification aimed to evaluate glass meltability, ease of extraction from the crucible, and suitability for industrial-scale production. Rapid quenching in water was employed to produce a granular glass material, referred to as frit.

2.3 | ABVF Aggregates Realisation

The ABVF matrix consists of approximately 85 wt% red clay, which enhances water retention and soil quality, making it suitable for both ornamental and agricultural applications. Clay plays a dual role: it improves soil structure and contributes to the gradual release of essential nutrients such as calcium, magnesium, potassium, and phosphates, thereby enhancing soil fertility. The remaining components of matrix are biochar (7.5% wt%) and SCGs (SCGs, 7.5% wt%), each providing specific functional benefits. Biochar serves to reduce bulk density and lighten the material while acting as a soil conditioner when applied in the field. Its high porosity improves water retention and nutrient availability, extending nutrient residence time in the root zone. In this formulation, biochar also raised the pH above 7. To counterbalance this effect in the raw formulation, SCGs were incorporated to adjust the pH toward neutrality. Biochar and SCGs are carbon-containing components which are oxidised and removed as gaseous products, mainly CO_2, during thermal treatment, creating additional porosity within the matrix.

To supply macronutrients (K_2O and P_2O_5), 30 parts by mass of glass frit were added to 100 parts of clay-biochar-SCGs matrix, corresponding to approximately 23.1 wt% glass frit in the final unfired formulation. Certain glass compositions are known to release nutrients gradually, functioning as glass-matrix fertilisers (GMFs). These systems enable controlled nutrient delivery and help maintain the biogeochemical balance of the soil-plant-ecosystem, thereby supporting sustainable and intensive agricultural practices [50].

For this study, the glass component was produced as frit in collaboration with Colorobbia Italia SpA (Sovigliana Vinci) using a semi-industrial melting furnace (operating at 1400°C for 1 h). Each batch consisted of 2 kg of raw mix per formulation. The raw materials, animal bone meal ash, pumice scraps, packaging glass cullet, and potassium carbonate (particle size < 1 mm), were homogenised and loaded into refractory crucibles. Several melting trials were performed by varying the glass cullet-to-pumice ratio to optimise meltability and facilitate glass extraction from the crucible while lowering the characteristic melting temperature. Rapid quenching in water was used to produce granular glass (frit) for subsequent mixing.

ABVF aggregates were produced by semi-industrial pelletization as cylindrical micropellets, 2.0–2.5 mm in diameter and 2–3 mm in length. The pellets were obtained by cold extrusion using an industrial pelletizer operated in collaboration with an industrial partner. This is a cold extrusion process, where the components (red clay, SCGs, and biochar with a maximum particle size of 1 mm, and fertilising glass powder with a maximum particle size of 100 μm) are dry-premixed and then moistened with water (up to 20 wt%) to obtain a paste suitable for extrusion. After extrusion, the pellets are dried at 50°C–60°C for 8 h. The dried product is then screened to remove particles outside the target size range. The final product has a moisture content of approximately 2%.

A portion of the dried micropellets was left unfired (raw), while another portion underwent firing in a static gas furnace (industrial firedamp) at 1000°C with a 30-min isothermal hold (visual representation of the pellets in Figure 1). This step aimed to enhance structural integrity through partial vitrification. Both the raw and fired ABVF formulations were retained for comparative analysis of physical, chemical, and nutrient-release properties.

The formulation was therefore designed as a multiphase architecture: the clay phase provides extrusion processability and fired mechanical integrity, the biochar and SCGs fractions act as pore-forming and soil-conditioning components, and the glass phase acts as the main PK reservoir.

2.4 | Fertiliser Glass Characterisation

The glass frit was characterised to determine its chemical and thermal properties. Chemical composition was measured using wavelength-dispersive X-ray fluorescence (WDXRF) with a PANalytical Zetium spectrometer, while characteristic thermal behaviour was evaluated by heating microscopy (HSM, Expert System Solutions, model M3MD1600/80/2) to identify key transformation temperatures.

2.5 | Matrix Raw Materials Characterisation

The reported Red Clay and SCGs characterisation was previously assessed by the authors [38, 51]. In this study, additional analyses were performed to characterise the biochar and assess its suitability as a fertiliser component, as well as its contribution to the ABVF system. Furthermore, the elemental composition (C, H, N, S wt%) was determined through CHNS analysis using a Thermo Scientific FLASH 2000 analyzer.

2.6 | ABVF Aggregates Characterisation

Fertiliser micropellets were analysed using various physical and chemical tests to verify their benefits and applications in agronomy and green roofs.

FIGURE 1 | Photos, respectively, of raw ABVF pellets (left) and fired ABVF pellets (right).

2.6.1 | *Physical Properties*

Tap density was determined using a Densi-Tap IG/4 device, with three replicates for each measurement. For each sample, both fired and unfired, 100 g of material was weighed and subjected to sequential tapping cycles of 10, 500, 1250, and 2500 taps. For the determination of the tap density value, the sample was subjected to tapping cycles up to the volume variation was less than 2 mL. The number of taps was considered enough when no significant volume reduction occurred [52].

From the data obtained, the following flowability indices were calculated: Hausner ratio (HR), using the Equation (1):

$$\mathrm{HR} = \frac{V_0}{V_{\mathrm{fin}}}, \tag{1}$$

and compressibility index (CI), obtained using the Equation (2):

$$\mathrm{CI} = \frac{(V_0 - V_{\mathrm{fin}}) \times 100}{V_0}, \tag{2}$$

where V_0 and V_{fin} are the initial and the final volumes (after the maximum number of taps used), respectively.

The bulk density and tap density were calculated using the following formula using the volumes measured in the tests (V) and the weight of the samples (W).

Bulk density = W/V_0,

Tap density = W/V_{fin}.

The physical characteristics measured are critical for storage, handling, and industrial processing of the material so very important for the scale up of the process.

Finally, the apparent density (ρ_a) was calculated from the mass to volume ratio of the sample, and the real density (ρ_r) was measured with a helium pycnometer (AccuPyc 1340, Micromeritics).

2.6.2 | *Mercury Intrusion Porosimetry (MIP)*

MIP was used to evaluate the pore size distribution, total porosity, and pore network characteristics of raw and fired ABVF micropellets. Measurements were carried out on the pellets without sectioning, using an AutoPore IV 9500 porosimeter (Micromeritics), operating over a pressure range from low pressure (down to 0.50 psia) up to high pressure (33,000 psia), allowing the investigation of pores spanning from the macroporous to the mesoporous regime.

Mercury surface tension was set at 485 dyn·cm^{-1}, with contact angles fixed at 130°. Intrusion data were processed according to the Washburn equation to calculate pore diameters. The measured parameters included cumulative intrusion volume, total pore area, median and average pore diameters, apparent (skeletal) and bulk densities, and open porosity. In addition, pore structure descriptors such as threshold pressure, tortuosity and permeability were determined.

Comparative analyses were performed on raw and fired ABVF micropellets to evaluate the effect of thermal treatment on pore architecture and transport-related properties relevant to water retention and nutrient diffusion.

2.6.3 | *Mass Loss in Water*

Mass loss tests were conducted in distilled water following D.Lgs. 75/2010 and European Regulation 2003/2003 [53] to assess material stability in neutral conditions. This static test was applied to both raw and fired ABVF samples as well as the five different glass formulations, using a 1:10 sample-to-solution ratio. Filtration was carried out after contact times of 1, 2, 4 h, 7, 14, and 28 days. Residual solids were dried at 100°C for 2 h, weighed to calculate weight loss (Equation 3).

$$\text{Undissolved (\%)} = \frac{\text{final mass (g)}}{\text{initial mass (g)}} \times 100. \tag{3}$$

The same procedure was repeated at each established sampling time.

2.6.4 | SEM

The surface morphology of the samples was examined by scanning electron microscopy using a JEOL JSM-6010LA microscope. Prior to observation, the samples were mounted on aluminum stubs and coated with a conductive carbon layer. Representative images were acquired at magnifications of ×50, ×700, and ×3000 at a working distance of 10 mm and a spot size setting of 30.

2.6.5 | XRPD

XRPD analyses were performed on the ABVF samples before and after firing, as well as on the different glass formulations, in order to evaluate their phase composition and the changes induced by thermal treatment. Diffraction patterns were collected using Empyrean MultiCore 3rd generation (Malvern Panalytical, Malvern, United Kingdom) diffractometer. The instrument is equipped with a Cu LFF HR (High Resolution) X-ray tube anode, including a Ni Beta filter, a 4 kW generator (set at 40 kV, 40 mA), and a PIXcel3D solid-state detector (Medipix3 technology). Samples were analysed using a side-loading sample holder. Data were acquired over a 2θ range of 5°–80°, with a step size of 0.0066° and a counting time of 55.85 s per step.

2.6.6 | Chemical Tests

Chemical characterisation of raw and fired ABVF micropellets included compositional and solubility analyses. The chemical composition was determined by WDXRF using a PANalytical Zetium spectrometer equipped with a WDS Zetium detector. Sample preparation involved pressing tablets consisting of 2.7 g of material and 0.27 g of wax on a boric acid bed into aluminum-supported pads, followed by compaction under a 150 kN load. Elemental analysis (C, H, N, S wt%) was carried out using a Thermo Scientific FLASH 2000 CHNS Analyzer.

Leaching tests were conducted to evaluate nutrient release behaviour under two simulated conditions: 2% m/v citric acid ($C_6H_8O_7$), representing rhizospheric conditions, and 0.5 M acetic acid (CH_3COOH), simulating acidic rain. In particular, citric acid solubility indicates the fraction of nutrients potentially available to plants due to its chelating properties, which mimic soil humic substances [38]. Many studies examine glass fertilisers solubility and slow release fertilisers nutrient release in citric acid to mimic the acidic conditions near plant roots that aid nutrient uptake [46, 47, 54–56], and citric-acid-extractable P specifically has been reported to correlate better to plant uptake than water-soluble P alone [57]. Conversely, acetic acid, as a non-chelating agent with low pH, reflects nutrient susceptibility to leaching under acidic conditions. Both tests were performed at pre-established contact times (30 min, 24 h, 7, 14, 21, 42, and 90 days), following official procedures: citric acid tests according to D.Lgs. 75/2010 [53] and acetic acid tests according to CNR IRSA Q 64 App. II Vol. 3 (1986) [58]. For each test, a dynamic approach was adopted using an Asal Universal Table Shaker 709 at 50 rpm, with a sample-to-solution ratio of 1:100. Three independent replicates were prepared for each contact time by weighing 1 g of sample (± 0.001 g) into 100 mL polyethylene beakers, adding citric or acetic acid solution to volume, and filtering through phosphate-free pleated filters (Ø130 mm) at the end of each period. Filtrates were analysed for pH (Hamilton Liq-Glass SL, OAKTON Eutech pH 5/6 and Ion 6), electrical conductivity (OAKTON Eutech CON6/TDS 6), and nutrient concentrations by ICP-MS. For consistency with fertiliser composition and regulatory reporting conventions, the releases of P, K, Mg, Ca, Al, and Fe were subsequently converted and expressed as oxide equivalents (P_2O_5, K_2O, MgO, CaO, Al_2O_3, and Fe_2O_3). The filters containing solid residues were dried at 105°C for 24 h and weighed to determine mass loss.

Regarding heavy metal analysis, there are no regulatory limits on release to soil in terms of flux or accumulation over time, which also depends on factors such as soil type, application frequency, and crops. However, Regulation (EU) 2019/1009 [59] sets maximum limits for contaminants (including heavy metals) in fertiliser products in the European Union.

2.6.7 | Kinetic Modelling

To interpret nutrient release, Phosphorus and Potassium release (expressed as P_2O_5 and K_2O relative % by weight) were fitted using a multi-model approach, consistent with recent literature recommendations for SRFs and CRFs [60].

Different models were employed: Higuchi, Korsmeyer-Peppas, Pseudo-first-order (PFO), and pseudo-second-order (PSO).

Higuchi model assumes pure Fickian diffusion from a matrix (migration from the inside of the material to the outside), described by Equation (4):

$$Q(t) = k_H\, t^{1/2}, \tag{4}$$

where $Q(t)$ = quantity released at time t, k_H = Higuchi diffusion constant, t = time. The model is based on the main assumptions that the material is uniformly distributed, diffusion is the dominant mechanism, the matrix does not dissolve rapidly, and the geometry of the system remains approximately constant.

The PFO model assumes nutrient release rate to be proportional to the remaining concentration in the matrix (Equation 5, integrated formula of PFO model):

$$Q(t) = Q\infty(1 - e^{-k_1 t}), \tag{5}$$

where $Q(t)$ = quantity released at time t, Q_∞ = equilibrium quantity (i.e., the maximum releasable fraction), k_1 = pseudo-first-order rate constant, $e^{-k_1 t}$ = exponential term that controls the speed, t = time. The physical interpretation of the model consists in the release rate depending strictly on the concentration of the substance remaining in the matrix. As the remaining amount decreases, the rate of release slows down proportionally.

PSO model has been shown to be a good kinetic descriptor for systems whose release or uptake is dominated by ion exchange [61–63], and it's expressed by the integrated formula reported in Equation (6):

$$Q(t) = \frac{Q\infty^2 k_2 t}{1 + Q\infty k_2 t}, \quad (6)$$

where $Q(t)$ = quantity released at time t, Q_∞ = equilibrium quantity (i.e., the maximum releasable fraction), k_2 = pseudo-second-order rate constant, t = time. The PSO model assumes that the process is controlled primarily by chemical interactions, surface-solute bonds, chemisorption, electron exchange, or strong interactions. For this reason, the PSO often describes experimental data better than the PFO.

Finally the Korsmeyer-Peppas model is a semi-empirical model based on the power function model, often used to fit nutrient release from polymeric coated systems [64], and described by Equation (7):

$$\frac{Q(t)}{Q\infty} = k_k t^n, \quad (7)$$

where $Q(t)$ = quantity released at time t, Q_∞ = maximum releasable fraction, k_k = Korsmeyer-Peppas rate constant, and n is the exponential factor, whose value is used to identify the release mechanism: for cylindrical pellets, $n < 0.45$ is associated with Fickian diffusion, $0.5 < n < 0.89$ indicates anomalous transport, often associated with a combination of mechanisms such diffusion and swelling or corrosion of the matrix, and $n > 0.89$ indicates Case-II transport (only swelling/relaxation-controlled) [65]. This model is more general and is useful when the release mechanism is not purely diffusive.

Oftentimes in composite systems different release mechanisms can coexist, such as dissolution, erosion, swelling, diffusion, ion exchange, absorption/desorption, depending on parameters such as the solubility, porosity and permeation characteristics of the matrix, and surrounding environment conditions. Kinetic model fitting is used in this work to identify the dominant mechanism when possible and evaluate differences depending on the aggregate state (raw vs. fired) and extraction media. Kinetic model fitting was performed in RStudio. The fitting procedure was applied to the release data of P and K, expressed as P_2O_5 and K_2O equivalent wt%, and the best-fitting model for each dataset was selected based on the highest R^2 and the lowest RMSE.

2.6.8 | *Antimicrobial Test*

Antimicrobial activity of raw and fired ABVF aggregates was provided by the laboratory of Engineering Campus of University of Campania. The antimicrobial properties were evaluated using the slightly modified Kirby-Bauer method [66]: bacterial pellets were dissolved in distilled saline water (0.9% NaCl) and diluted to obtain bacterial suspensions of 10^5 CFU/mL, which were then plated on appropriate solid agar media. The bacteria used for this test were both Gram-negative (*Escherichia coli*, *Pseudomonas aeruginosa*) and Gram-positive (*Enterococcus faecalis*, *Clostridium perfringens*). Before incubation, 200 and 300 mg of compressed sample powder, with 1.3 cm of diameter, were sterilised under UV light for 1 h and placed at the centre of Petri dishes (PPD). The incubation conditions were as follows: *E. coli* at 44°C for 24 h, *C. perfringens* at 44°C for 24 h under anaerobic conditions, and *E. faecalis* and *P. aeruginosa* at 36°C for 48 h. After incubation, the diameters of the inhibition zones were measured and recorded in relation to the 6 cm Petri dish diameter. All the experimental procedure has been performed in triplicate.

2.6.9 | *Field Trials: Growth Tests*

The agronomic performances were assessed at the Minoprio Foundation in Vertemate con Minoprio (CO), certified laboratory. Preliminary growth tests were carried out to evaluate any stimulating or depressive effects of the two innovative fertilising systems (raw and fired). The test was conducted taking as a reference the method used to evaluate the depressing or biostimulating effects of composted matrices [67]. The tests were performed following non-phytotoxicity results performed by the same laboratory. From 1.25 to 10 g of fertiliser were added to 1 kg of substrate with a predominantly sandy matrix (as indicated in the norm). Each experimental thesis involved four replicates, represented by four pots with a diameter of 8 cm, in each of which two lettuce plants with the first true leaf were transplanted. The pots were placed in a controlled environment and water regime, with a light cycle of 16 h day and 8 h night. Cultivation was suspended after 21 days, and the fresh weight and dry weight (75°C) of the aerial plant biomass produced by each replicate were determined.

In view of the favourable results obtained with the fired system, an experimental trial was conducted in a period from June to November to evaluate the use of fired ABVF aggregates as an innovative fertiliser system in growing substrates for green roofs. The test involved the cultivation of two plant species: ornamental meadow with microtherm species (a mix of *Festuca arundinacea* and *Poa pratensis*) in sod; ornamental shrub *Photina X Fraseri* (pot diameter 16 cm). Cultivation was carried out in plastic boxes measuring 770 × 550 × 305 mm, inside which two cultivation substrates were placed: A (control) = vulcaflor intensive substrate (a commercial volcanic mineral substrate composed of pumice and lapillus) supplemented with a standard NPK fertiliser (3 kg/m^3), and B (new fertiliser) = vulcaflor intensive substrate with fired ABVF fertiliser (3 kg/m^3). The choice of an NPK-based control was intentional, as nitrogen is also an essential macronutrient for plant growth; this setup allows us to evaluate the performance of our PK system in comparison to a complete nutrient solution, with the expectation that its agronomic results will be at least comparable. The field trial was designed as a practical performance comparison between a commercial complete fertilisation regime and the experimental fired ABVF formulation under the same substrate and application rate (3 kg/m^3), rather than as a nutrient-balanced equivalence test. The ornamental lawn was watered by sprinkling, while the photinia was watered by drip irrigation. The tests were carried out during three surveys: after 2 months, after 4 months, and at the end of the experiment after 6 months. The parameters were: data collection of fresh and dry biomass production and aesthetic index (colour, vigour, cover) for the meadow; and height, number of main branches, chlorophyll II content, fresh and dry biomass/container (only after 6 months) for the photinia; at the beginning of the trial the height of the individual plants was also surveyed in order to determine the growth data in the subsequent surveys.

3 | Results and Discussion

3.1 | Fertiliser Glass

The fertiliser glass previously developed by the authors on laboratory scale by melting a batch of 100 g in a small refractory crucible, using an electric elevator furnace with a thermal cycle of 4–5 h up to the melting temperature of 1400°C [38], proved unsuitable for casting during the prototyping test. These tests were carried out on a 2000 g batch melted in a mullite crucible using a static furnace ("grisolera") equipped with a gas-air burner system, with the crucible inserted directly into the furnace at 1400°C for 60 min. The grisolera is the kiln used for the development of new ceramic frits and glazes prior to industrial-scale production by the industrial partner. Consequently, a series of tests were carried out under the same operating conditions, while modifying the formulation, particularly the ratio of fluxing raw materials, without changing the nutrient content. The specific aim was to evaluate the scalability of the product and optimise the glass formulation for large-scale production. In these trials, only the flux component has been modified, systematically varying the ratio between glassy sand (derived from packaging glass cullet) and pumice scraps. Table 1 summarises the five tested compositions, in which pumice content increased progressively from 20 wt% in Trial 1 to 40 wt% in Trial 5 (the one that replicates the formulation tested in the laboratory), along with the corresponding chemical and thermal properties.

The five frit formulations exhibited a clear relationship between composition and thermal processability. As the pumice fraction increased from Trials 1 to 5, Al_2O_3 increased from 4.63 to 7.96 wt%, while Na_2O decreased from 3.40 to 1.37 wt%; over the same series, the characteristic temperatures shifted upward, with softening increasing from 1244°C to 1401°C and melting from 1389°C to 1434°C. This trend indicates progressively lower fusibility and less favourable melting behaviour under the adopted semi-industrial conditions.

XRPD analysis (Figure 2) further supported this evidence. All frit formulations showed reflections attributable to $Na_2Ca_4(PO_4)_2SiO_4$, indicating the formation of a common silicophosphate phase during synthesis. In contrast, reflections attributable to $Ca_5(PO_4)_3OH$ were observed only in Trials 3–5, with increasing intensity, and were absent in Trials 1 and 2. This phase is likely associated with residual calcium phosphate inherited from the bone meal ash precursor. Its persistence in the more pumice-rich formulations suggests less complete dissolution or reaction of the precursor phase during melting, consistent with their poorer fusibility. On this basis, Trial 1 was selected as the glassy fertiliser component for subsequent ABVF preparation because it showed the most favourable combination of thermal behaviour, phase evolution, and operational feasibility during semi-industrial melting. By heating microscopy, used as a comparative experimental approach to evaluate processability-related behaviour, Trial 1 was identified as the optimal compromise between meltability, thermal stability, and operational feasibility based on its lower characteristic temperatures and superior melting behaviour. Hot-stage observations supported this interpretation, as Trial 1 showed earlier deformation and yielding under its own weight (particularly at the softening point), whereas the more pumice-rich

TABLE 1 | XRF and heating microscope data of the different fertiliser glass compositions realised.

Glass composition	XRF analysis									Characteristic temperatures		
	Al_2O_3 (wt%)	SiO_2 (wt%)	Na_2O (wt%)	MgO (wt%)	P_2O_5 (wt%)	TiO_2 (wt%)	K_2O (wt%)	CaO (wt%)	Fe_2O_3 (wt%)	Total	Sintering (°C)	Softening (°C)	Melting (°C)
1	4.63	25.85	3.40	1.08	17.61	0.19	15.67	29.98	1.26	99.72	1147	1244	1389
2	5.23	24.19	2.73	0.93	17.37	0.25	16.60	30.69	1.63	99.66	1140	1333	1407
3	6.07	23.97	2.34	0.89	17.70	0.26	16.82	29.76	1.85	99.71	1206	1364	1421
4	6.96	23.10	1.86	0.85	18.12	0.31	17.14	29.19	2.10	99.66	1223	1345	1427
5	7.96	22.39	1.37	0.86	18.02	0.34	17.22	29.11	2.36	99.67	1280	1401	1434

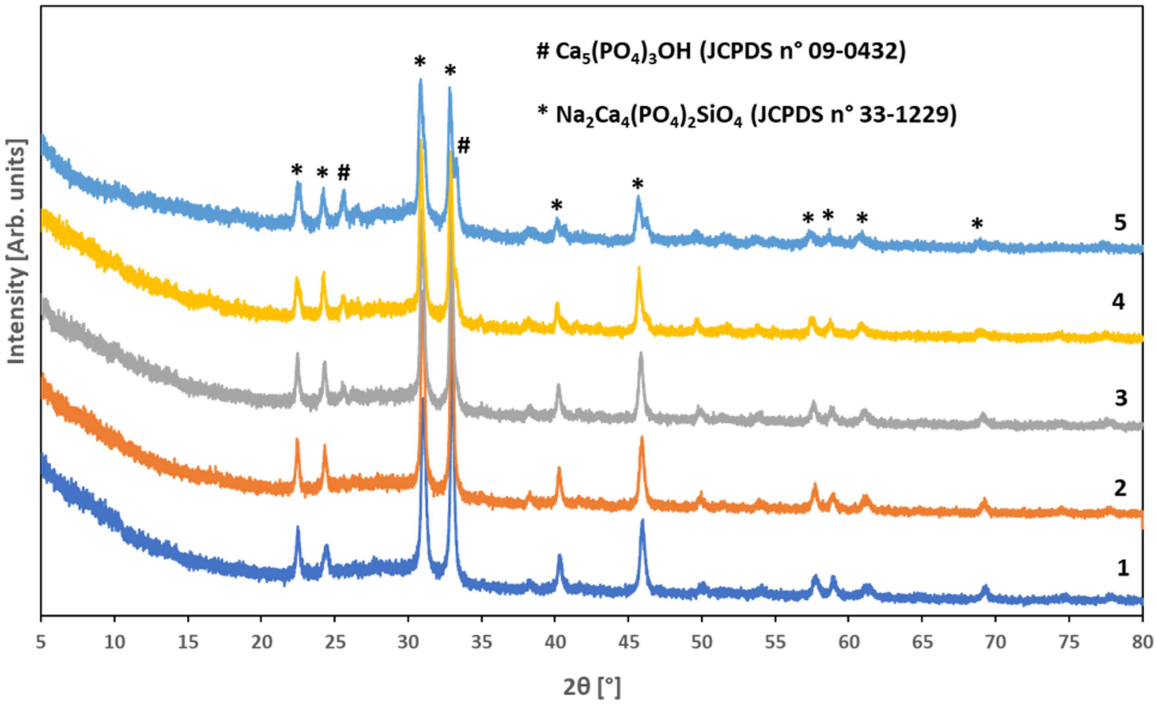

FIGURE 2 | XRPD patterns of the five glass formulations (Trials 1–5).

TABLE 2 | Elemental composition of biochar used (elements are expressed in wt%).

Sample	N	C	H	S
Biochar	0.21	82.08	1.26	—
SCGs	2.27	48.67	6.54	—
Red clay	—	0.84	0.75	—

TABLE 3 | Chemical analysis (XRF) of red clay and SCGs.

Oxide [wt%]	Red clay	SCGs	Biochar
SiO_2	52.77	0.37	0.70
Al_2O_3	17.95	0.03	0.12
Fe_2O_3	7.89	0.02	0.08
MgO	3.88	0.17	0,14
K_2O	2.85	0.58	0,36
CaO	2.57	0.19	1,39
TiO_2	0.78	0.01	0.00
Na_2O	0.66	0.14	0,04
MnO	0.19	0.00	0.03
P_2O_5	0.00	0.32	0,08
L.O.I. (1050°C)	9.90	98.05	95.4

formulations retained their shape longer during heating. This behaviour is consistent with the compositional evolution of the glasses from Trials 1 to 5, particularly the gradual decrease in Na_2O and the increase in pumice-derived refractory oxides, especially Al_2O_3, which are typically associated with reduced fluxing action and poorer melt flowability.

3.2 | Matrix Raw Materials Characterisation

The red clay used is a ferruginous clay. XRPD analysis indicate the presence of the crystalline phases: quartz (SiO_2), kaolinite ($Al_2Si_2O_5(OH)_4$), illite ($KAl_2Si_3AlO_{10}(OH)_2$), expandable smectite minerals (e.g., montmorillonite, $(Na,Ca)_{0.33}(Al,Mg)_2Si_4O_{10}(OH)_2{\cdot}nH_2O$), calcium and magnesium carbonate (dolomite ($CaMgCO_3$), and hematite (Fe_2O_3) [51].

Biochar, red clay, and SCGs [38] elemental analysis is reported in Table 2, while XRF data are listed in Table 3.

The nitrogen content in biochar is generally low because, during pyrolysis under oxygen-limited conditions, most nitrogen compounds in the original biomass are volatilised as gases. The hydrogen-to-carbon (H/C) ratio is often used as an indicator of biochar stability: a low H/C ratio suggests enhanced structural stability and reduced susceptibility to degradation, reflecting efficient pyrolysis that removes volatile components and leaves primarily fixed carbon [66]. Furthermore, the absence of sulphur makes biochar suitable for agricultural applications without posing risks of soil acidification or increased salinity.

Based on the nominal formulation used for ABVF preparation, corresponding to approximately 65.4 wt% red clay, 5.8 wt% biochar, 5.8 wt% SCGs, and 23.1 wt% glass frit, the origin of the main oxides can be estimated from the XRF composition of the individual raw materials (see Table 4). SiO_2 is mainly supplied by the red clay (~85%), with a secondary contribution from the glass frit (~15%). Al_2O_3, Fe_2O_3, TiO_2, MnO, and most MgO also derive predominantly from the red clay (~92%, ~95%, ~92%, ~100%, and ~91%, respectively). In contrast, P_2O_5 is almost entirely supplied by the glass frit (~99%), as well as CaO is mainly associated with the glass phase (~80%), reflecting the Ca-rich raw materials used for frit preparation. K_2O has a mixed origin, with the glass frit providing the main contribution

TABLE 4 | Estimated source attribution of the main oxides in ABVF (expressed as wt% in final batch) based on nominal formulation and raw-material XRF data.

Oxide	From red clay	From SCGs	From glass Trial 1	From Biochar	Calculated total	Main source
SiO_2	34.50	0.02	5.97	0.04	40.53	Mostly red clay
Al_2O_3	11.74	0.00	1.07	0.01	12.82	Mostly red clay
Fe_2O_3	5.16	0.00	0.29	0.00	5.45	Mostly red clay
MgO	2.54	0.01	0.25	0.01	2.81	Mostly red clay
K_2O	1.86	0.03	3.62	0.02	5.54	Mainly glass, secondary clay
CaO	1.68	0.01	6.92	0.08	8.69	Mainly glass
TiO_2	0.51	0.00	0.05	0.00	0.56	Mostly red clay
Na_2O	0.43	0.01	0.79	0.00	1.23	Mainly glass, secondary clay
MnO	0.12	0.00	0.00	0.00	0.12	Red clay
P_2O_5	0.00	0.02	4.07	0.00	4.09	Almost entirely glass

TABLE 5 | Physical properties of raw and fired ABVF micropellets.

Sample	Hausner ratio (HR)	Compressibility index (CI) (%)	Bulk density (g/mL)	Tap density (g/mL)
Raw ABVF	1.11	9.8	0.822	0.912
Fired ABVF	1.10	9.2	0.769	0.848

TABLE 6 | Apparent and real densities measured.

Sample	Apparent density ρ_a (g/cm^3)	Real density ρ_r (g/cm^3)
Raw ABVF	1.28	2.53
Fired ABVF	1.41	2.68

(~66%) and the red clay a secondary contribution (~34%), likely from K-bearing aluminosilicate phases. SCGs and biochar contribute negligibly to inorganic oxides.

3.3 | ABVF Aggregates Characterisation

3.3.1 | *Physical Properties*

In the context of material handling and storage for the studied samples, TAP density measurements were performed to determine two indices reflecting the flowability and compressibility of micropellets. Tables 5 and 6 report the values of the parameters previously described for each kind of micropellets measured.

From the obtained results, the raw micropellets show a slightly higher CI respect to the fired one. This difference can be explained by the fact that the raw material was only pelletized and not fired and, therefore, had not undergone thermal densification, making it more easily compressible. According to the literature [68], a CI between 1% and 10% corresponds to excellent flowability, and a HR value between 1.00 and 1.11 correspond to excellent flow, whereas values above 1.60 indicate very poor flowability. In general, high HR values indicate a greater difference between the tap and bulk density, which is a sign of increased inter-particle cohesion and poor flow. For the reported samples, the values of tap and bulk densities were similar (around 0.8 g/mL), which is consistent with high flowability. The specific HR depends on factors such as particle size, shape and moisture content and it is not an intrinsic property of the material itself. This behaviour is advantageous from an industrial perspective, as it facilitates handling, storage, transport, and dosing of the pellets.

3.3.2 | *Mercury Intrusion Porosimetry*

MIP revealed significant differences in pore structure between raw and fired ABVF micropellets, confirming that thermal treatment modifies the pore network while preserving overall porosity. Both materials exhibited high open porosity, with values of approximately 35.8% for raw ABVF and 36.8% for fired ABVF, indicating that firing does not lead to pore collapse but rather to pore redistribution. The micro-pellets were measured as-is without breaking or sectioning them; therefore, the measured porosity was primarily open porosity, to evaluate factors such as permeability, water retention, and nutrient release.

Despite similar total intrusion volumes (0.242 $mL \cdot g^{-1}$ for raw and 0.246 $mL \cdot g^{-1}$ for fired samples), evident changes were observed in pore size distribution and pore surface area. Raw ABVF showed a higher total pore surface area (10.70 $m^2 \cdot g^{-1}$) compared to the fired material (1.38 $m^2 \cdot g^{-1}$).

Firing induced a shift of the pore size distribution toward larger pore diameters. This is supported by the smaller average pore diameter (4 V/A) in raw micropellets (0.091 μm) relative to fired ones (0.714 μm) and the increase in median pore diameter by

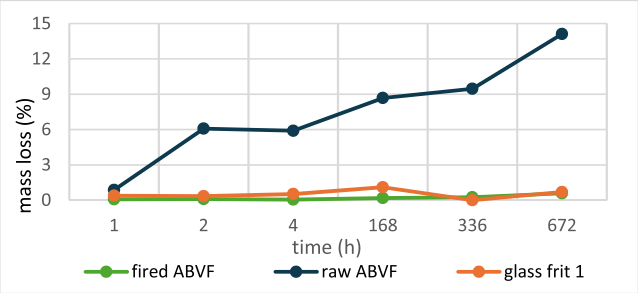

FIGURE 3 | Trend of mass loss in deionized water of ABVF samples (fired and raw), and of the glass frit by increasing contact time.

volume from 0.30 μm in the raw state to 2.90 μm after firing. This pore coarsening can be attributed to the combustion of carbonaceous components (SCGs and biochar).

The pore network topology also evolved with firing. The raw ABVF exhibited higher permeability (≈1200 mD) compared to the fired sample (≈400 mD), consistent with a highly connected network of fine pores facilitating fluid intrusion. After firing, the decrease in permeability indicates a more diffusion-limited pore system, despite the presence of larger pores. This behaviour can be attributed to the formation of a viscous glassy phase during thermal treatment, which partially seals surface-accessible porosity. At the same time, the decomposition of pore-forming agents promotes the formation of larger intra-aggregate pores, leading to pore coarsening within the microstructure. This interpretation is supported by comparable tortuosity values for both samples, indicating that thermal treatment does not disrupt pore connectivity but limits fluid transport through the narrowing or elimination of flow-effective pore throats, a structural evolution which is expected to slow down nutrients diffusion. Overall, MIP results demonstrate that firing transforms the ABVF micropellets from a highly microporous, high-surface-area system into a material dominated by larger, more stable pores with lower surface area and permeability.

3.3.3 | *Mass Loss in Water*

Mass loss experiments in water (Figure 3) further corroborate the structural interpretation derived from microstructural and porosimetric analyses.

The fired ABVF exhibited a small initial mass loss, followed by a slow and limited increase over time, reaching approximately 0.59 wt%. Remarkably, the glass frit displayed a very similar dissolution trend, with a final mass loss of about 0.7 wt%. Although the fertiliser glass represents only a fraction of the fired formulation, this convergence seems to confirm that firing leads to the formation of a continuous glass-ceramic matrix that governs the overall dissolution behaviour. In contrast, the raw ABVF exhibited a sharp mass loss within the first hours of immersion, followed by a continuous increase reaching approximately 14 wt% after prolonged contact.

This behaviour is attributed to the lack of structural consolidation in the raw aggregates, which promotes rapid water penetration, progressive disintegration of less stable phases, and enhanced exposure of soluble glass particles and other labile components. The marked difference between raw and fired formulations highlights the critical role of firing-induced vitrification in enhancing structural integrity, reducing the immediate availability of soluble phases, and aligning the dissolution behaviour of the composite aggregate with that of a durable glass frit.

3.3.4 | *SEM*

SEM observations (Figure 4) indicate that thermal treatment modifies the microstructure of the ABVF micropellets, confirming mercury porosimetry data. In the raw sample, the matrix appears finer and more compact, with a pore network dominated by smaller voids. After firing, the microstructure becomes coarser, and the pores appear larger and more clearly defined, particularly at higher magnification. This evolution is consistent with pore coarsening induced by thermal treatment, which can be attributed to the burnout of organic components such as SCGs and biochar.

3.3.5 | *XRPD*

The XRPD patterns of raw and fired ABVF (Figure 5) highlight the structural changes induced by thermal treatment. Raw ABVF exhibits a more crystalline profile, with numerous sharp reflections attributable to mineral phases inherited from the clay-rich matrix, especially muscovite, kaolinite, albite, dolomite, and illite, as well as to the added fertiliser glass phase $Na_2Ca_4(PO_4)_2SiO_4$; the main peaks used for mineral identification are reported in Table 7. The most intense reflections are associated with quartz. After firing, the diffractogram becomes less sharp and shows a more pronounced diffuse contribution, indicating partial vitrification. In particular, the clay-related crystalline phases and the $Na_2Ca_4(PO_4)_2SiO_4$ phase disappear, while quartz reflections are still retained, with lower intensity, indicating that firing at 1000°C does not produce a fully amorphous material.

3.3.6 | *Chemical Tests*

Raw and fired ABVF chemical analysis (XRF) reported in Table 8 shows that the main oxides present in both samples are silica (SiO_2) followed by alumina (Al_2O_3), both coming from the predominant clay component, which provides the aluminosilicate matrix. Other main oxides are CaO, K_2O, and P_2O_5 provided by the fertiliser glass added. Raw sample shows a loss on ignition (L.O.I) of 17.64%. The values in the fired ABVF sample are higher due to concentration phenomenon due to firing, except for chlorine and Cu which decrease, and for Pb for which the concentration in the fired ABVF falls under the limit of detection. This means that a significant portion of the weight of the original sample consisted of volatile components (water, organic compounds or other substances that decompose or evaporate at high temperatures). During sintering, these materials are removed, reducing the total weight of the sample. The removal of moisture and volatile substances during sintering increases the relative concentration of oxides such as P_2O_5, K_2O, MgO, and CaO, which are essential for plant nutrition. From an industrial and

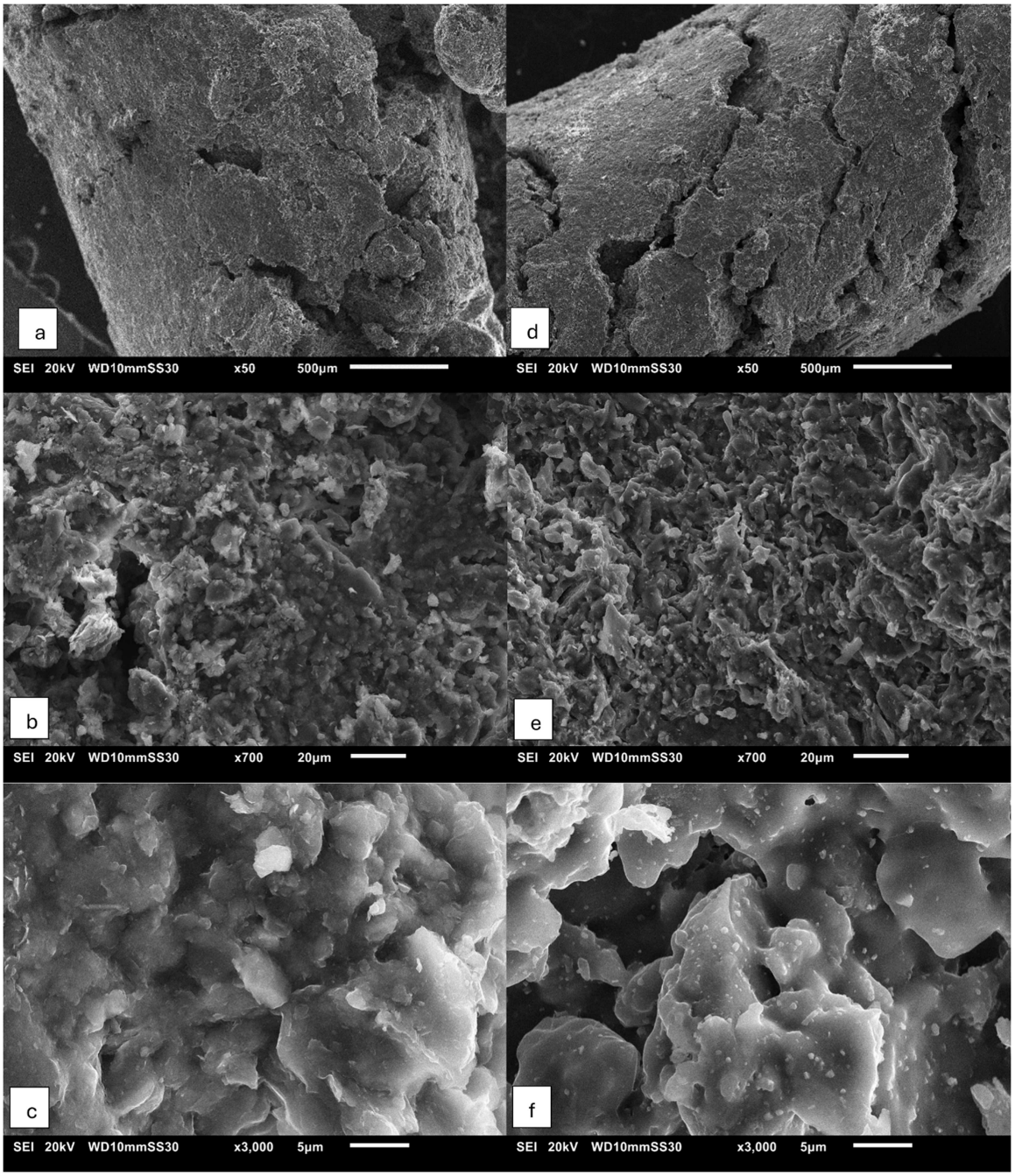

FIGURE 4 | SEM images of raw and fired ABVF micropellets at increasing magnification. Raw pellets: ×50 (a), ×700 (b), and ×3000 (c). Fired pellets: ×50 (d), ×700 (e), and ×3000 (f).

economic perspective, this is advantageous because it produces a more nutrient-dense product, reducing transportation, storage, and application costs.

Considering the formulation includes waste-derived feedstocks, reproducibility of the final composition requires routine control of raw-material chemistry, especially the glass frit composition, clay mineralogy, organic matter content, and trace-element levels. In this study, the final ABVF aggregates showed heavy-metal contents below the relevant regulatory limits, supporting the environmental suitability of the selected raw-material combination.

Leaching tests were performed to evaluate the release capacity of both raw and fired ABVF micropellets in two different acid extractants and depending on the contact time.

Figure 6 reports the apparent dissolved P and K fractions, expressed as P_2O_5 and K_2O equivalents, measured in the extracting solutions at each contact time. The extraction solutions were analysed after finite contact times, which means the profiles represent the net amount of nutrient remaining in solution rather than strictly cumulative release. Results are expressed as percent oxides with respect to total content by weight, measured in the initial samples by XRF technique.

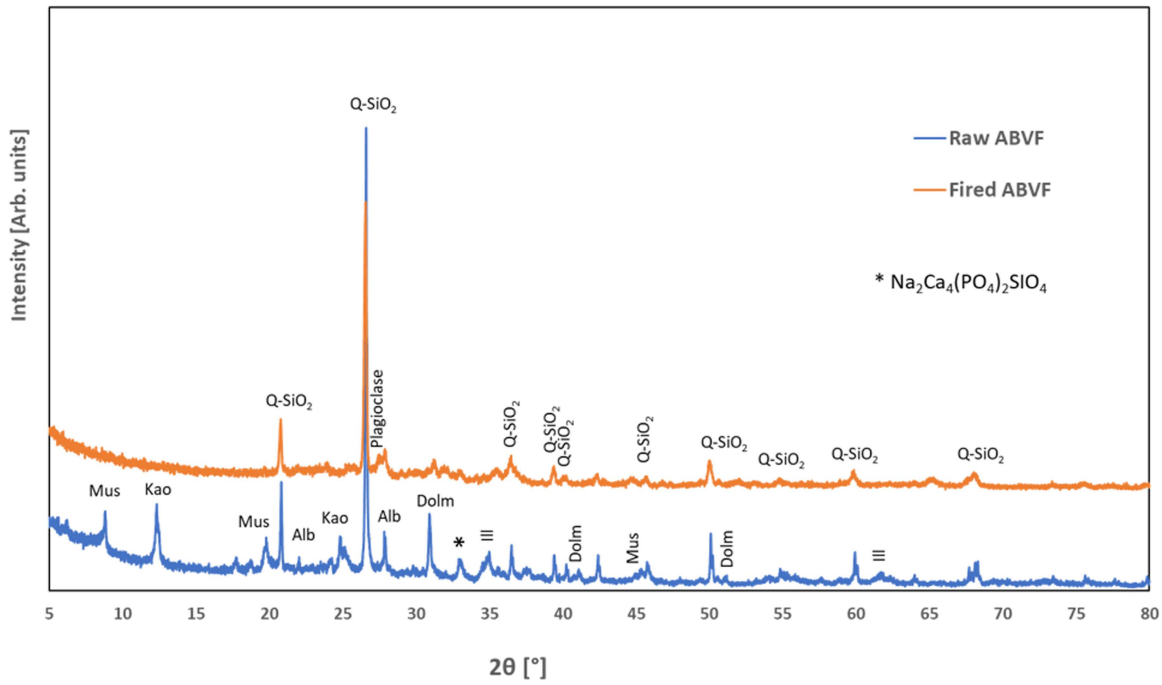

FIGURE 5 | XRPD pattern of ABVF micropellets before and after firing.

TABLE 7 | Main XRPD peaks used for phase identification in raw and fired ABVF.

Sample	2θ Position (°)	d-Spacing (A°)	Miller indices (hkl)	Assigned phase
Raw ABVF	8.89	9.95	(002)	Muscovite $KAl_2(AlSi_3O_{10})(OH)_2$
Raw ABVF	17.81	4.98	(004)	Muscovite $KAl_2(AlSi_3O_{10})(OH)_2$
Raw ABVF	35.98	2.50	(131)	Muscovite $KAl_2(AlSi_3O_{10})(OH)_2$
Raw ABVF	12.35	7.16	(001)	Kaolinite $Al_2Si_2O_5(OH)_4$
Raw ABVF	24.88	3.58	(002)	Kaolinite $Al_2Si_2O_5(OH)_4$
Raw ABVF	19.78	4.48	(020)	Illite $K_{0.65}Al2[Al_{0.65}Si_{3.35}O_{10}](OH)_2$
Raw ABVF	34.90	2.57	(112)	Illite $K_{0.65}Al2[Al_{0.65}Si_{3.35}O_{10}](OH)_2$
Raw ABVF	61.30	1.51	(060)	Illite $K_{0.65}Al2[Al_{0.65}Si_{3.35}O_{10}](OH)_2$
Raw ABVF	26.64	3.34	(101)	Quartz SiO_2
Raw ABVF	20.85	4.26	(100)	Quartz SiO_2
Raw ABVF	50.14	1.82	(112)	Quartz SiO_2
Raw ABVF	27.52	3.24	(201)	Albite $NaAlSi_3O_8$
Raw ABVF	22.03	4.03	(002)	Albite $NaAlSi_3O_8$
Raw ABVF	30.96	2.89	(104)	Dolomite $(Ca,Mg)CO_3$
Raw ABVF	41.14	2.19	(113)	Dolomite $(Ca,Mg)CO_3$
Raw ABVF	50.54	1.80	(116)	Dolomite $(Ca,Mg)CO_3$
Raw ABVF	32.24	2.77	(230)	$Na_2Ca_4(PO_4)_2SiO_4$
Fired ABVF	26.64	3.34	(101)	Quartz SiO_2
Fired ABVF	20.85	4.26	(100)	Quartz SiO_2
Fired ABVF	50.14	1.82	(112)	Quartz SiO_2
Fired ABVF	27.52	3.24	(201)	Plagioclase $Ca_{0.64}Na_{0.32}Al_{1.775}Si_{2.275}O_8$
Fired ABVF	27.48	3.24	(201)	Anortoclase $(Na_{0.75}K_{0.25})AlSi_3O_8$

To gain mechanistic insight regarding the two macronutrients release, four kinetic models, Higuchi, PFO, PSO, and Korsmeyer-Peppas were used to fit the data. The fitting parameters for each model are listed in Table 9.

The nutrient release behaviour of ABVF aggregates results from the superposition of physical and chemical control mechanisms intentionally introduced through material design. As widely reported for slow- and controlled-release fertilisers based on mineral, glassy, or

TABLE 8 | XRF analysis of raw and fired ABVF micropellets.

Raw ABVF		Fired ABVF	
Oxide	**Concentration (%)**	**Oxide**	**Concentration (%)**
SiO_2	41.48	SiO_2	47.71
Al_2O_3	14.99	Al_2O_3	17.02
CaO	6.56	CaO	8.85
K_2O	6.12	K_2O	8.23
Fe_2O_3	5.61	Fe_2O_3	7.94
P_2O_5	3.07	P_2O_5	4.30
MgO	2.49	MgO	3.47
Na_2O	0.87	Na_2O	1.02
TiO_2	0.77	TiO_2	0.96
MnO	0.17	MnO	0.19
Element	**Concentration (ppm)**	**Element**	**Concentration (ppm)**
Cl	514 ppm	Cl	459 ppm
S	314 ppm	S	524 ppm
Rb	252 ppm	Rb	313 ppm
Sr	246 ppm	Sr	332 ppm
Ba	189 ppm	Ba	311 ppm
Zr	180 ppm	Zr	258 ppm
Cr	160 ppm	Cr	195 ppm
Zn	114 ppm	Zn	141 ppm
Co	< 15 ppm	Co	132 ppm
Ni	90 ppm	Ni	98 ppm
Pb	74 ppm	Pb	< 30 ppm
Cu	75 ppm	Cu	71 ppm
As	< 5 ppm	As	< 5 ppm
Cd	< 10 ppm	Cd	< 10 ppm
Ga	34 ppm	Ga	42 ppm
Y	22 ppm	Y	30 ppm
Nb	15 ppm	Nb	27 ppm
LOI (%)	17.64	LOI (%)	0

composite matrices, nutrient release is rarely governed by a single process, but rather by the coupled action of diffusion, solid-state dissolution, ion exchange, and interfacial interactions, whose relative contribution depends on nutrient speciation, matrix structure, and extraction conditions [21].

In the present system, two main barriers contribute to release control. The first is a physical barrier, related to the existence of a consolidated granular structure characterised by pore size distribution, tortuosity, and diffusion length. MIP, SEM, and XRPD observations show that firing induces partial vitrification of the clay-glass composite, leading to a reduction in open and interconnected porosity, disappearance of the finest pores, and lower permeability. These changes increase diffusion path length and limit mass transport from the bulk of the aggregates to the solution. The second barrier is chemical, associated with the incorporation of nutrients into mineral or glass networks and reversible interactions with charged or functional surfaces provided by clay minerals, biochar, and residual organic matter. The relative importance of these mechanisms differs between phosphorus and potassium due to their distinct chemical roles within the matrix.

Phosphorus in ABVF aggregates is introduced almost exclusively through the fertiliser glass, where it acts as a network-forming species (P–O–P and P–O–M bonds) [46] with only minor contributions from residual crystalline calcium phosphate phases. Consequently, phosphorus release is intrinsically linked to glass corrosion and network dissolution [47], rather than to ion exchange or surface desorption mechanisms. This interpretation is supported by kinetic results. Under all tested conditions, P release is better described by the PFO model, indicating that the release rate is primarily proportional to the amount of phosphorus remaining within the solid matrix. Such behaviour is characteristic of systems in which solid-state dissolution and diffusion through the matrix constitute the rate-limiting steps, and has already been observed in phosphate glasses [60, 69].

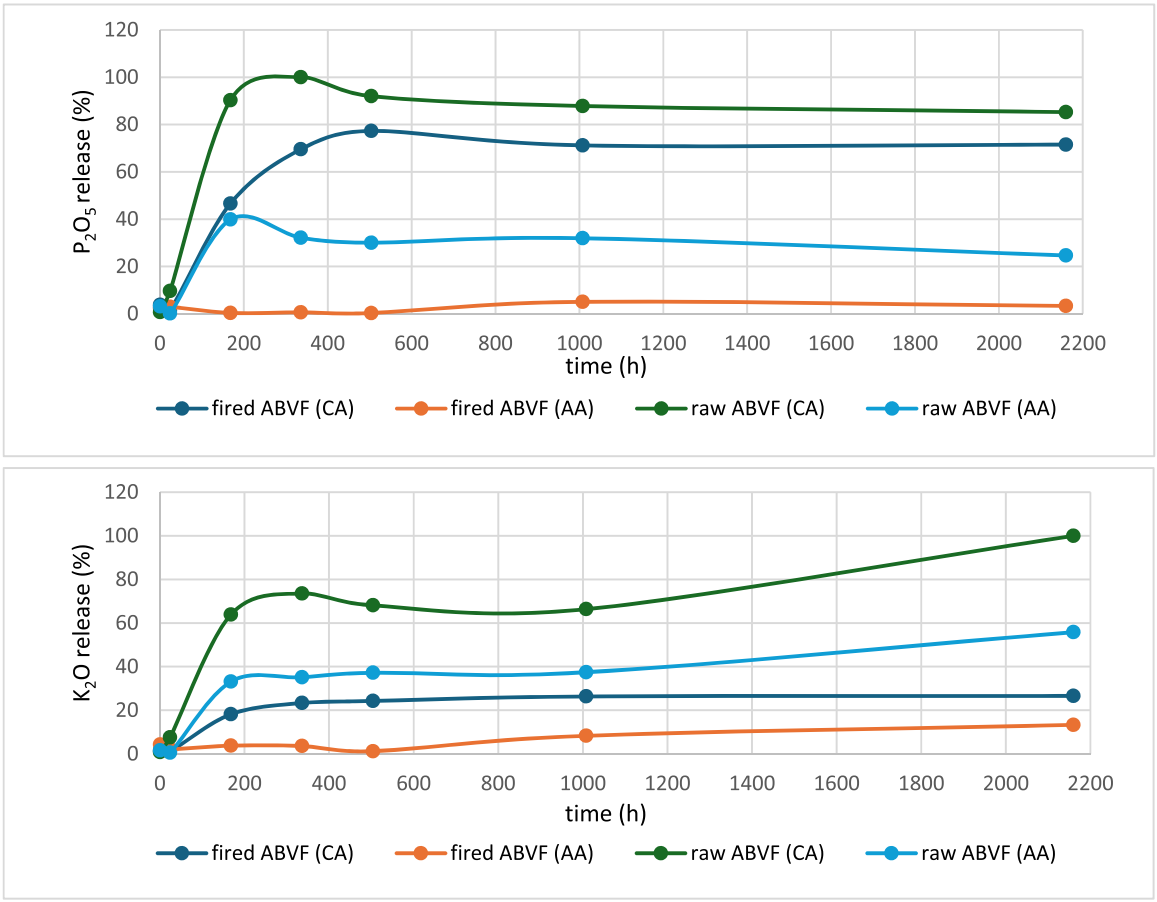

FIGURE 6 | P and K release expressed as P_2O_5 and K_2O equivalents (relative wt%) for fired and raw ABVF for both release environments (AA = acetic acid and CA = citric acid).

TABLE 9 | Kinetic fitting parameters for each model of P and K release expressed as P_2O_5 and K_2O equivalents (%).

Models	Higuchi		PFO		PSO		Korsmeyer-Peppas		
Parameters	R^2	RMSE	R^2	RMSE	R^2	RMSE	R^2	RMSE	n_{est}
P_2O_5—raw ABVF (CA)	0.9063	13.839	0.9472	8.9831	0.9129	12.5956	0.8922	14.8439	0.750
P_2O_5—fired ABVF (CA)	0.9406	7.7873	0.9679	5.4724	0.9218	9.1776	0.9451	7.4913	0.518
P_2O_5—raw ABVF (AA)	0.6928	8.9873	0.8098	6.202	0.7399	7.8270	0.6670	9.3287	0.300
P_2O_5—fired ABVF (AA)	n.c.	n.c.	n.c.	n.c.	n.c.	n.c.	n.c.	n.c.	n.c.
K_2O—raw ABVF (CA)	n.c.	n.c.	0.8229	14.1735	0.8995	11.4968	0.7662	16.2889	0.208
K_2O—fired ABVF (CA)	0.8467	4.1172	0.9846	1.2945	0.9753	1.7801	0.8352	4.2685	0.253
K_2O—raw ABVF (AA)	0.8048	6.6896	0.8557	7.1419	0.9285	5.3521	0.8596	7.0449	0.277
K_2O—fired ABVF (AA)	0.5924	2.4858	0.6325	2.3604	0.6991	2.2104	0.6570	2.2803	0.660

Note: n.c. = no convergence. Model fitting did not converge despite increasing the maximum number of iterations, indicating that the model was not suitable to describe the release profile.

The release curves exhibit a non-monotonic increase followed by a plateau. In CA the release stabilises around 90% by weight of the total P_2O_5 for the raw ABVF and 70% for the fired ABVF after 21 days. In acetic acid, the released amounts were significantly lower: raw ABVF released only 30%–35% of P_2O_5, while the fired formulation showed minimal solubility under these conditions. The non-monotonic behaviour is consistent with solution saturation and secondary precipitation phenomena, as further supported by XRPD analyses after 21 days of immersion, which reveal the formation of hydroxyapatite phases on the aggregates surface. This effect is slightly more pronounced in raw ABVF, where higher Ca^{2+} availability and greater glass exposure, due to the less consolidated and more permeable structure, enhance phosphate precipitation.

The stronger extraction observed in citric acid compared to acetic acid further confirms that P release is controlled by glass dissolution. Citric acid promotes corrosion of the aluminosilicate-phosphate network by chelating multivalent cations (Ca^{2+}, Al^{3+}, Fe^{3+}) [70], destabilising the glass structure.

Citric acid release profiles in fact, are described by values of $n > 0.45$ in the Korsmeyer-Peppas model, consistent with anomalous transport, and a mixed mechanism of diffusion and possibly matrix corrosion. After firing, diffusion through the densified matrix becomes increasingly limiting, especially in acetic acid.

Regarding K_2O release, in citric acid raw ABVF exhibited an initial rapid release of K_2O, reaching ~80% within 14 days, then stabilising before ultimately achieving complete release (100%) between 42 and 90 days. In acetic acid the release was more modest but still eventually reached 60% with the same trend profile. Conversely, the fired formulation showed lower release in both media, plateauing at approximately 25% after 14 days in citric acid, in contrast to the 17% in acetic acid reached at the end of the experiment. In contrast to phosphorus, potassium in raw ABVF aggregates exists in multiple reservoirs characterised by different mobilities. These include exchangeable K associated with clay mineral surfaces (illite-smectite fraction), biochar and organic matter functional groups, and glass surfaces, non-exchangeable K residing in interlayer positions of clay minerals, and structurally bound K, acting as a network-modifying cation within the glass. This heterogeneous distribution results in the experimentally observed multi-stage release pattern, similar in both extractant solutions. The early stage is dominated by ion exchange at external and readily accessible sites, while the later stages reflect gradual mobilisation of less accessible and partially fixed potassium [46, 71]. In this context, the PSO model mostly provides the best overall description of K release kinetics in both citric and acetic acid, coherent with the hypothesis that the release rate depends on the progressive depletion of exchangeable and reversibly bound K sites rather than on simple matrix-regulated diffusion. Comparable K-release kinetics have been reported for clay-bearing calcareous systems, with PSO behaviour giving a stronger overall fit [71]. Thermal treatment fundamentally alters these mechanisms. Firing induces dihydroxylation, collapse of clay lamellar structures, partial melting and vitrification, as confirmed by the disappearance of clay diffraction peaks in XRPD patterns and by microstructural observations. Therefore, classical ion-exchange reservoirs are less dominant, and potassium becomes increasingly structurally embedded. Its release is governed primarily by slow glass corrosion and diffusion through the new structure, resulting in lower cumulative release and the disappearance of the second release step. For fired micropellets, under strong chelating conditions (citric acid), PFO provides a slightly better description of the release behaviour than PSO model, which could indicate that glass corrosion is sufficiently rapid that K exposure is not the limiting step. Under non-chelating conditions (acetic acid), corrosion is slower and K release becomes controlled by interfacial processes at the hydrated glass surface, explaining the persistence of PSO-dominated behaviour even in fired aggregates. A clear distinction emerges between phosphorus and potassium release mechanisms. For phosphorus, the nature of the extractant plays a dominant role, with citric acid consistently promoting higher release than acetic acid in both raw and fired aggregates. This reflects the structural incorporation of P within the glass network, whose dissolution is strongly enhanced by chelation of multivalent cations. In contrast, potassium release is primarily governed by the structural state of the aggregates. Raw samples systematically display higher cumulative K release compared to fired ones in both extractants, indicating that matrix consolidation and loss of exchangeable phases upon firing represent the main limiting factors. The distinct kinetic behaviour observed for P and K further supports that nutrient speciation within the matrix, rather than porosity alone, governs the release mechanism. Figure 7 shows the release over time of dissolved Mg, Al, Ca, and Fe, measured by ICP-MS and expressed as MgO, Al_2O_3, CaO, and Fe_2O_3 equivalents, respectively, in relative percentage by weight respect to the initial content in the two extraction media.

Citric acid exhibited higher extractive capability for all elements on both raw and fired ABVF, characterised by a slightly non-monotonic behaviour more evident for CaO, compatibly with the precipitation of calcium phosphate phases hypothesised by P_2O_5 decreasing concentration mainly starting at 336 h and further evidenced by XRPD results. Citric acid ability to form stable complexes likely accounts for its effectiveness in breaking down aluminosilicate phases and mobilising phosphorus. This is agronomically relevant because such complexation processes can occur in the rhizosphere, where organic acids from root exudates improve nutrient availability.

Raw ABVF releases were generally higher and less delayed in both media and, except for Fe_2O_3, differences in the total released amount for each cation between the two media are less pronounced. This behaviour mirrors the macronutrient release trends and further confirms that the fired glass-ceramic structure is less susceptible to dissolution driven either by chelation or by pH effects. The larger fluctuations observed in acetic acid are due to the fact that dissolution is mainly controlled by acidity and released Ca^{2+} and phosphate species are more susceptible to saturation and precipitation. In citric acid, citrate ligands enhance glass-network corrosion by complexing Ca^{2+}, Al^{3+}, and Fe^{3+}, but they also stabilise released cations, making concentration profiles less controlled by immediate precipitation.

Figure 8 shows the evolving of pH and specific conductivity of the solutions in time for both ABVF samples, as further verification of the release behaviour. Trends are shown with respect to a control acetic acid (AA) and citric acid (CA) without aggregate contact.

The evolution of pH and electrical conductivity provides additional mechanistic insight into nutrient release. In acetic acid, marked differences emerge between raw and fired aggregates: raw ABVF induces a pronounced and non-monotonic pH evolution, initially driven by ion-exchange and glass dissolution processes, resulting in a transient pH increase. This is followed by a pH decrease concomitant with the depletion of Ca and P from solution and the crystallisation of calcium phosphate phases, as confirmed by XRPD evidence of hydroxyapatite (see Supporting Information S1: Figure S1 in the Supporting Information Material). The pH decrease is interpreted as a consequence of hydroxyapatite precipitation [72], rather than

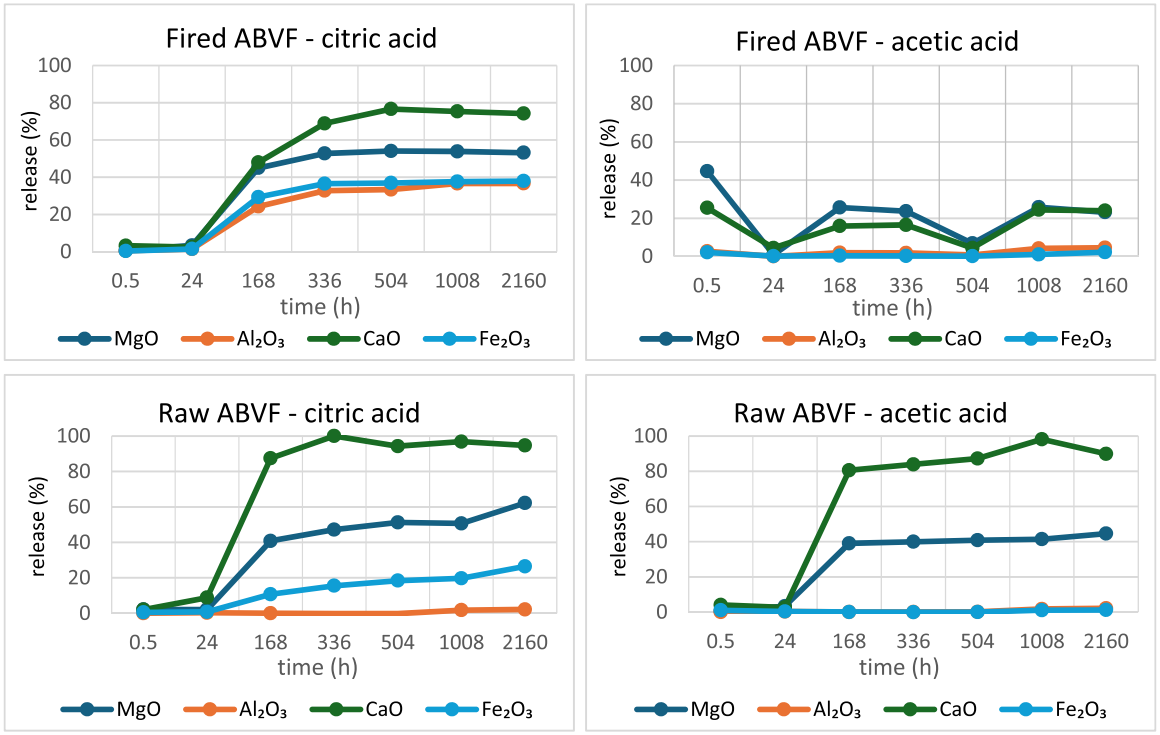

FIGURE 7 | Elements release expressed as oxide equivalents (wt%) for fired and raw ABVF in citric acid (CA) and acetic acid (AA).

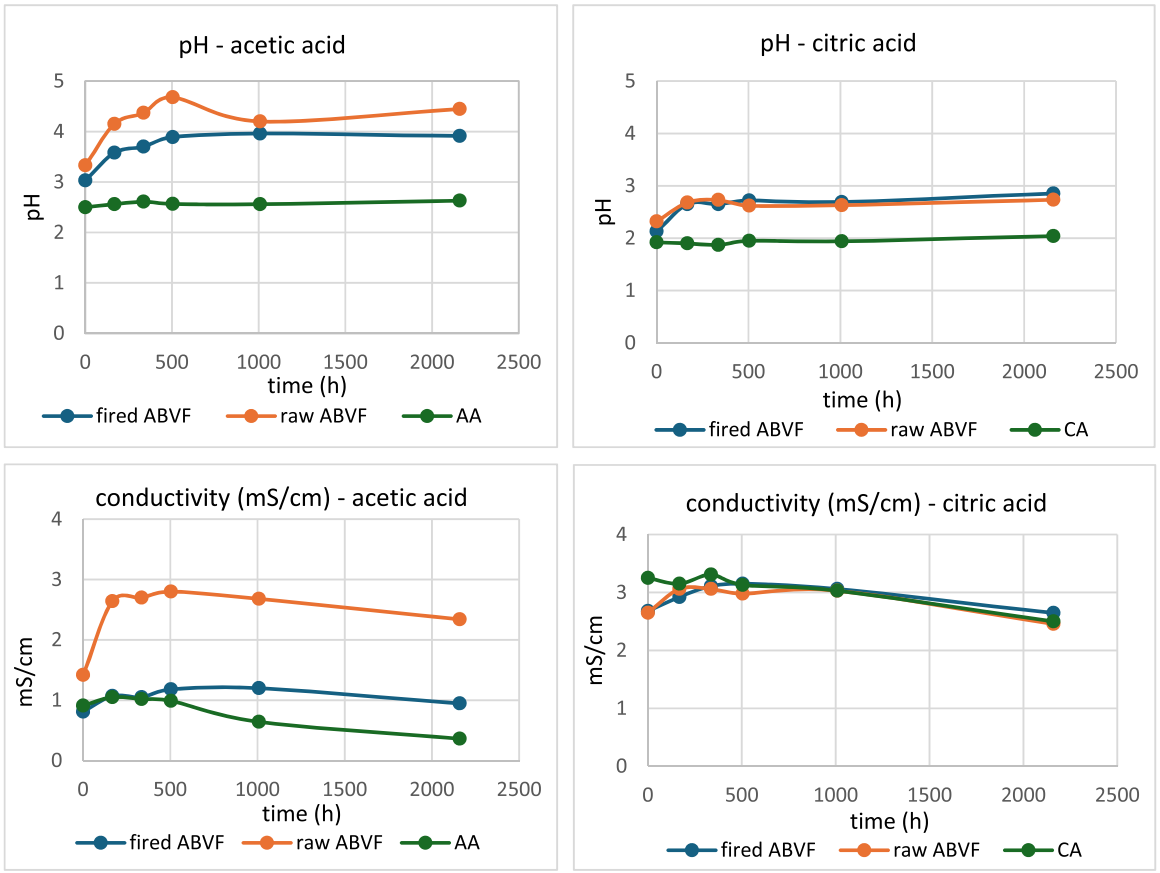

FIGURE 8 | pH value trend over time and specific conductivity (mS/cm) trend over time.

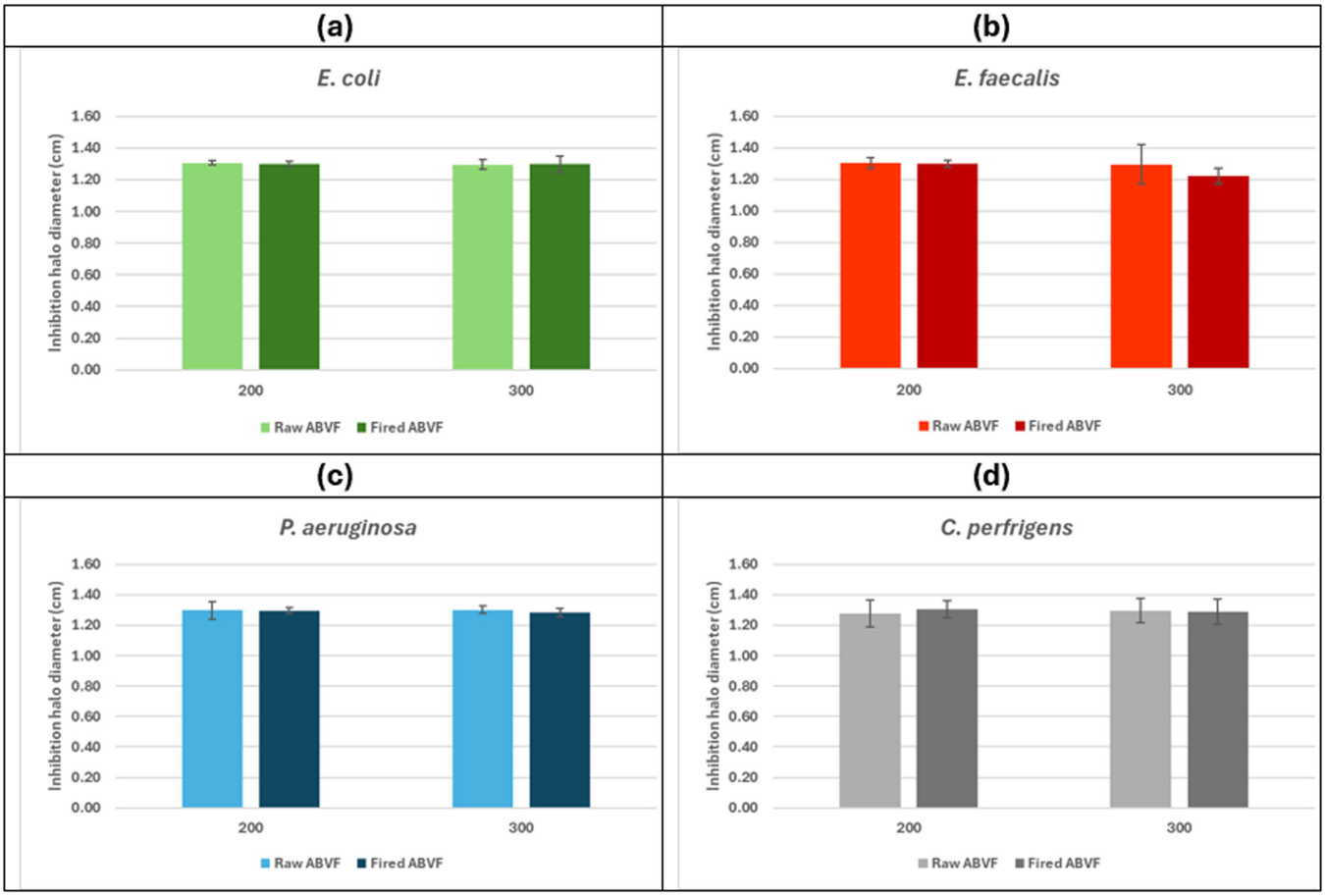

FIGURE 9 | Inhibition halo diameters recorded after incubation of 200 and 300 mg of raw and fired ABVF with (a) *E. coli*, (b) *E. faecalis*, (c) *P. aeruginosa*, and (d) *C. perfrigens*.

its driving force. This decrease can be explained both through hydrogen ions (H^+) release, or consumption of hydroxide ions (OH^-), making the environment more acidic. A simplified precipitation reaction is:

$$5\ Ca^{2+} + 3\ PO_4^{3-} + OH^- \rightarrow Ca_5(PO_4)_3OH_{\downarrow,}$$

from which it can be seen that: hydroxyapatite crystals generate from calcium, phosphate, and hydroxide ions; the reaction consumes OH^- ions and this removal shifts the balance toward a higher concentration of H^+. In aqueous phosphate systems, there is also another important equilibrium:

$$HPO_4^{2-} \rightleftharpoons PO_4^{3-} + H^+.$$

When PO_4^{3-} is removed to form hydroxyapatite, this equilibrium shifts to the right to produce more phosphate ions, and this releases additional H^+ ions into solution, further lowering the pH.

Fired ABVF shows a smaller pH increase and faster stabilisation, consistent with the reduced accessibility of reactive sites, together with the complete collapse of the original clay structure during firing and its incorporation into an amorphous glass-ceramic matrix, which led to lower overall ion release. Conductivity trends mirror this behaviour, with an initial increase, more pronounced for raw ABV, driven by the formation of mobile ionic species through exchange reactions, followed by a decrease as exchangeable reservoirs are depleted.

In contrast, citric acid solutions exhibit much smaller pH variations and similar trends for raw and fired aggregates despite markedly higher ion release and mass loss in the raw formulations. This reflects the strong chelating action of citrate, which promotes glass corrosion while limiting pH shifts and converting released cations into less mobile metal-citrate complexes [73], supporting the claim that solution supersaturation governs precipitation, while pH variations reflect the associated acid-base equilibria.

3.3.7 | *Antimicrobial Test*

Antimicrobial activity of ABVF samples was evaluated, with a view to sustainable application and industrial-scale production. During storage of the material, it is important that it does not develop a reaction to any bacteria or mould. Similarly, when applying ABVF micropellets in a soil system as fertiliser, it is important that they react positively to possible bacterial action [74]. The results of the antimicrobial activity are presented in Figure 9a–d. As observed, both raw and fired ABVF exhibited antimicrobial activity. The dimensions of the inhibition halos were like the diameter of the sample tablets (1.3 cm), indicating that,

while the antimicrobial activity is limited, bacteria were unable to grow in direct contact with the materials. Neither the ABVF sintering nor the amount tested resulted in any changes in the size of the inhibition halos. This indicates that the materials' antimicrobial properties are not dose-dependent and remain unaffected by heat treatment. These results are consistent if considering that: (i) the XRF analysis of both raw and fired ABVF revealed presence of heavy metal is in traces; (ii) firing treatments only remove some organic fraction resulting in an increase in sample porosity and produce amorphous samples. Starting from these considerations, the antimicrobial activity of the raw ABVF is linked to its composition and crystalline phases. Raw ABVF is primarily composed of clay, which has been reported to exhibit antimicrobial properties against various bacteria and pathogens, including *Escherichia coli* and *Pseudomonas aeruginosa* [75]. This activity is attributed to the crystalline phases within the clay and its composition, typically containing multiple metal oxides. Raw ABVF crystalline phases such as illite and kaolinite may contribute directly to antimicrobial effects by mechanically impacting bacterial cell walls. These crystals, with their sharp edges and unique surface properties, can physically damage bacterial membranes, enhancing antimicrobial activity even when chemical mechanisms are less pronounced. At elevated temperatures, however, clays lose their original crystalline structure and transform into metal oxides and other chemically stable forms [76]. In addition to clay, raw ABVF contains other components in smaller quantities, including coffee grounds, biochar, and fertiliser glass (a mixture of bone ash, pumice, and recycled glass). These components contribute to the antimicrobial activity through distinct mechanisms. Coffee grounds have demonstrated antimicrobial activity against both Gram-positive and Gram-negative bacterial strains [77]. This is primarily due to the presence of caffeic acid, a compound capable of penetrating bacterial cell walls and inhibiting DNA synthesis. This inhibition disrupts the synthesis of essential structural and functional proteins, such as enzymes critical for bacterial metabolism [78]. However, the antimicrobial effect of caffeic acid in these samples is limited due to the small quantities used. Furthermore, its effectiveness is likely restricted to the raw ABVF sample, as caffeic acid begins to degrade at 200°C. Despite the loss of crystallinity, fired ABVF can still influence the environment in ways that lead to bacterial cell death. Indeed, some metal concentration (such as Ba, Zr, Cr, Zn, Co, Ni) increased after firing. Their metal oxides can generate reactive oxygen species (ROS), such as hydroxyl radicals, through redox reactions like the Fenton reaction. These ROS are highly antimicrobial, causing extensive damage to DNA, proteins, and cell membranes, thereby maintaining the antimicrobial effectiveness of the thermally treated samples [79].

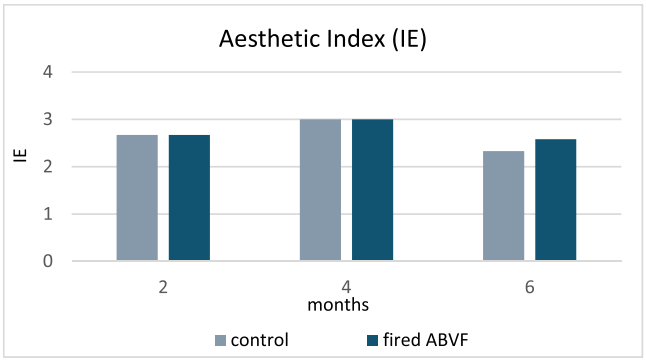

FIGURE 10 | Aesthetic Index (IE) of ornamental meadow.

3.3.8 | *Field Trials: Growth Tests*

The preliminary growth test to evaluate any stimulating or depressive effects allowed to verify that the different dosages of the two types of experimental fertilisers did not cause phytotoxic effects. More consistent results were obtained with fired ABVF and on this system we proceeded with the 6-month outdoor test on the two species.

Tests performed in the field provided results of different parameters for both types of plants: ornamental meadow (a mix of *Festuca arundinacea* and *Poa pratensis*) and *Photinia fraseri*. The treatment named "control" was performed using Vulcaflor intensive as substrate doped by standard basic NPK fertiliser (3 kg/m^3) while treatment B consist in Vulcaflor intensive substrate with fired ABVF fertiliser (3 kg/m^3).

In the field trial on ornamental meadow turfgrass, the fired ABVF showed comparable establishment to the NPK-fertilised control in the early stages. Over the 6-month observation period (with evaluations at 2, 4, and 6 months), both treatments supported healthy turf growth without visible nutrient deficiencies. Figure 10 illustrates the turf aesthetic index scores, which were initially the same for ABVF and control. By the final collecting

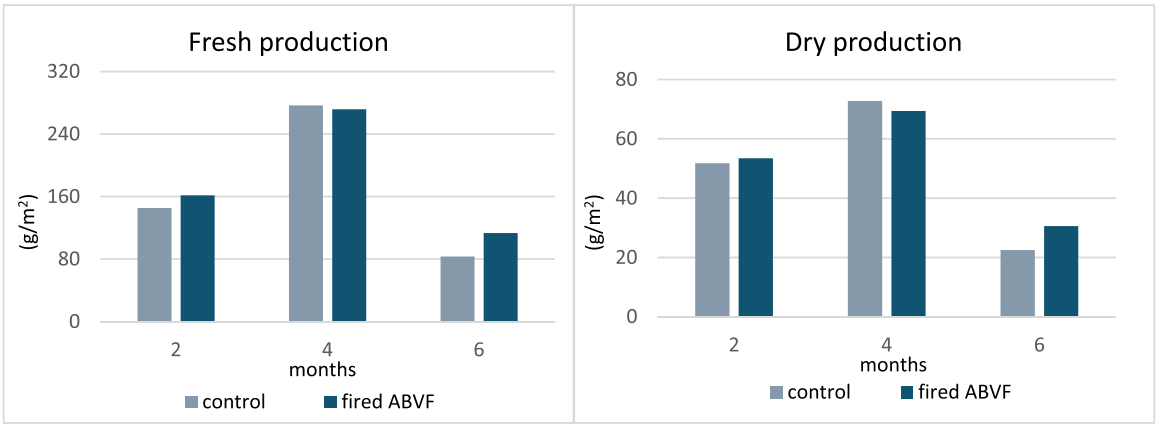

FIGURE 11 | Fresh and dry production of ornamental meadow (g/m^2).

at 6 months, the turf receiving ABVF had a higher aesthetic index than the control, indicating a denser, greener turf.

Figure 11 presents turfgrass biomass production [fresh and dry yield, in (g/m^2)]: the ABVF treatment achieved equal or greater biomass than the NPK treatment at the first and last time point. By the end of the trial, turfgrass fertilised with ABVF produced a higher fresh biomass yield than the conventional fertiliser. Dry matter yield followed a similar trend.

Overall, the turfgrass results indicate that the fired ABVF fertiliser can support equal or better lawn development compared to a standard NPK fertiliser in one application, especially over longer time trials (e.g., 6 months), validating its agronomic effectiveness for ornamental greenery.

The *Photinia fraseri* trial monitored plant height, branching development, chlorophyll content, and above-ground biomass at 2, 4, and 6 months. As shown in Figure 12, plant height increased progressively in both treatments. During the establishment phase, the ABVF treatment resulted in slightly reduced growth, possibly related to the absence of nitrogen in the ABVF treatment, together with the controlled-release behaviour of P and K, which limited their immediate availability.

As the season advanced, however, the progressive nutrient dissolution increasingly supported plant requirements, reducing the performance gap relative to the NPK control. Toward the end of the trial (October–November), growth slowdown was observed in both treatments due to seasonal effects.

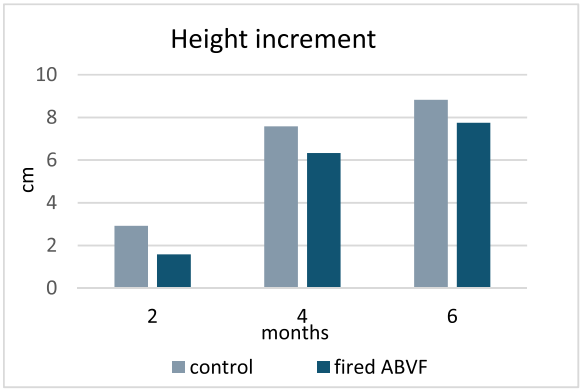

FIGURE 12 | Height increment of photinia (cm).

Figure 13 reports two other structural and physiological indicators: number of main branches per plant and leaf chlorophyll content. Photinia shrubs receiving ABVF initially showed fewer branches compared with the control, but this difference narrowed at later surveys, indicating that sustained nutrient release contributed to maintaining plant development. A similar pattern was recorded for chlorophyll concentration (mg/m^2), which improved gradually over time under the ABVF treatment and reached values comparable to those of the NPK control in the final survey. This outcome suggests that the maintained P and K availability helped preserve leaf functionality and plant vigor even if absence of externally supplied nitrogen in the ABVF formulation.

This comparison should be interpreted with caution because ABVF is a nitrogen-free PK fertiliser, whereas the control received a conventional NPK fertiliser; moreover, background substrate nitrogen availability and mineralisation were not quantified. Within these limits, the 6-month trial still shows that fired ABVF was able to sustain progressive plant development and to approach comparable end-of-trial biomass, branching, and chlorophyll status, supporting its use as a PK component in nutrient management systems where nitrogen is supplied separately or is already available in the substrate.

4 | Conclusions

This work addressed a concrete barrier to the industrial translation of a previously patented system: the original glass formulation exhibited viscosity and melting behaviour incompatible with semi-industrial processing conditions. By systematically modifying the glass composition (limited to the flow component only and maintaining the same macronutrient intake of P_2O_5 in the range of 17%–18% and K_2O in the range of 16%–17%), a frit was identified that allowed the entire production cycle (melting, cold extrusion, and firing) to be successfully executed using standard industrial machinery, and the resulting ABVF systems demonstrated mechanical stability, functional porosity, and regulatory compliance regarding heavy metals.

Functional validation revealed that firing slowed phosphorous release in citric acid (rhizosphere-proxy) by approximately 2 weeks,

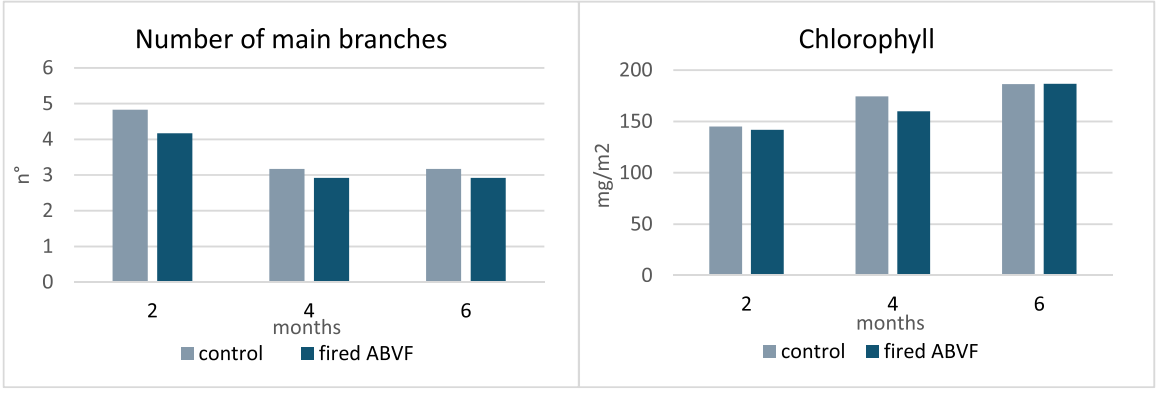

FIGURE 13 | Number of main branches and chlorophyll value (mg/m^2) of photinia.

while still reaching only slightly lower final release value compared to the raw-ABVF (~72% vs. ~85%), and the kinetic studies as well as structural evidence suggest that this is due to the less accessible matrix structure. On the other hand, the firing process seems to alter potassium speciation by collapsing exchangeable sites and structurally embedding K within the new glass-ceramic matrix. This limits potassium availability over the observed timeframe, causing its release to plateau at ~25% by 90 days.

Preliminary agronomic trials showed that the sustained release did translate into practical plant nutrition comparable to a conventional NPK fertiliser over a 6-month period, and antimicrobial testing and heavy-metal analyses confirmed compliance with safety requirements. Taken together, these results establish ABVF as a processable, safe, and agronomically effective PK system for integrated nutrient management strategies.

This outcome is achieved through a production model that relies on residues and EoW streams sourced from local Italian industries in the ceramic, quarrying, and agri-food sectors, a concrete example of local industrial symbiosis. Integrating co-located residues into a PK fertiliser can reduce dependence on finite mined phosphate and potash, contributing to circular nutrient flows, and represent an input for a more sustainable and resource-efficient agriculture.

However, a techno-economic assessment, including energy consumption assessment and cost analysis, and a life-cycle assessment will be necessary to evaluate whether the model proposed in this study is environmentally and economically viable at commercial scale, particularly given the energy demands of the frit production and firing steps. Optimising potassium availability through further glass and porous-structure engineering, and characterising nutrient bioavailability under realistic soil conditions, remain additional priorities for future work.

Acknowledgements

Special thanks to the Italian companies that supported the research by supplying raw materials and services: Europomice srl of Milan, Colorobbia Italia Spa of Sovigliana Vinci (FI) and Fiorano Modenese (MO), Clever Bioscience srl of Campospinoso Albaredo (PV), Minoprio Analisi e Certificazioni srl of Vertemate con Minoprio (CO). This work was supported by Proof of Concept Project "Lightweight fertilising materials and insulating polymer panels from char waste"—"PNRR Mission 1, Component 2, Investment 6, NextGenerationEU"—within the Program "Proof of Concept Empowering and Speeding-up Technology Evolution" (PoC ESTE).

Conflicts of Interest

The authors declare no conflicts of interest.

Data Availability Statement

The data that support the findings of this study are available from the corresponding author upon reasonable request.

References

1. N. Bechtaoui, M. K. Rabiu, A. Raklami, K. Oufdou, M. Hafidi, and M. Jemo, "Phosphate-Dependent Regulation of Growth and Stresses Management in Plants," *Frontiers of Plant Science* 12 (2021): 679916, https://doi.org/10.3389/fpls.2021.679916.

2. Y. Poirier, A. Jaskolowski, and J. Clúa, "Phosphate Acquisition and Metabolism in Plants," *Current Biology* 32 (2022): R623–R629, https://doi.org/10.1016/j.cub.2022.03.073.

3. F. Khan, A. B. Siddique, S. Shabala, M. Zhou, and C. Zhao, "Phosphorus Plays Key Roles in Regulating Plants' Physiological Responses to Abiotic Stresses," *Plants* 12 (2023): 2861, https://doi.org/10.3390/plants12152861.

4. Y. Wang, Y.-F. Chen, and W.-H. Wu, "Potassium and Phosphorus Transport and Signaling in Plants," *Journal of Integrative Plant Biology* 63 (2021): 34–52, https://doi.org/10.1111/jipb.13053.

5. J. Arbačauskas, Z. J. Vaišvila, G. Staugaitis, L. Žičkienė, A. Masevičienė, and D. Šumskis, "The Influence of Mineral NPK Fertiliser Rates on Potassium Dynamics in Soil: Data From a Long-Term Agricultural Plant Fertilisation Experiment," *Plants* 12 (2023): 3700, https://doi.org/10.3390/plants12213700.

6. R. B. Chowdhury, G. A. Moore, A. J. Weatherley, and M. Arora, "Key Sustainability Challenges for the Global Phosphorus Resource, Their Implications for Global Food Security, and Options for Mitigation," *Journal of Cleaner Production* 140 (2017): 945–963, https://doi.org/10.1016/j.jclepro.2016.07.012.

7. G. M. Filippelli, "Balancing the Global Distribution of Phosphorus With a View Toward Sustainability and Equity," *Global Biogeochemical Cycles* 32 (2018): 904–908, https://doi.org/10.1029/2018GB005923.

8. J. Baker, N. Schunk, M. Scholz, et al., "Global-to-Local Dependencies in Phosphorus Mass Flows and Markets: Pathways to Improving System Resiliency in Response to Exogenous Shocks," *Environmental Science & Technology Letters* 11 (2024): 493–502, https://doi.org/10.1021/acs.estlett.4c00208.

9. J. Rodeja, F. Coello, J. Sardans, and J. Penuelas, "The Potash Trilemma: Geopolitics, Market Dynamics, and Global Food Security," *Journal of Sustainable Agriculture and Environment* 4 (2025): e70050. https://doi.org/10.1002/sae2.70050.

10. H. Tayibi, M. Choura, F. A. López, F. J. Alguacil, and A. López-Delgado, "Environmental Impact and Management of Phosphogypsum," *Journal of Environmental Management* 90 (2009): 2377–2386, https://doi.org/10.1016/j.jenvman.2009.03.007.

11. H. Hamamo, S. Landsberger, G. Harbottle, and S. Panno, "Studies of Radioactivity and Heavy Metals in Phosphate Fertilizer," *Journal of Radioanalytical and Nuclear Chemistry* 194 (1995): 331–336, https://doi.org/10.1007/BF02038431.

12. Ş. Turhan, E. M. Altuner, A. Ayata, et al., "Dispersion of Oxides, Heavy Metals, and Natural Radionuclides in Phosphogypsum Stockpiles of the Phosphate Industries in Türkiye," *Environmental Science and Pollution Research* 32 (2025): 7692–7704, https://doi.org/10.1007/s11356-025-36180-2.

13. N. Ahmad, M. Usman, H. R. Ahmad, M. Sabir, Z. U. R. Farooqi, and M. T. Shehzad, "Environmental Implications of Phosphate-Based Fertilizer Industrial Waste and Its Management Practices," *Environmental Monitoring and Assessment* 195 (2023): 1326, https://doi.org/10.1007/s10661-023-11958-4.

14. L. K. Roesel, "Effects of Less Impermeable Sealings for Mine Piles," *Ecological Engineering* 176 (2022): 106515, https://doi.org/10.1016/j.ecoleng.2021.106515.

15. M. Cañedo-Argüelles, S. Brucet, S. Carrasco, et al., "Effects of Potash Mining on River Ecosystems: An Experimental Study," *Environmental Pollution* 224 (2017): 759–770, https://doi.org/10.1016/j.envpol.2016.12.072.

16. R. Ladrera, M. Cañedo-Argüelles, and N. Prat, "Impact of Potash Mining in Streams: The Llobregat Basin (Northeast Spain) as a Case Study," *Journal of Limnology* 76 (2017): 1525. https://doi.org/10.4081/jlimnol.2016.1525.

17. S. E. Haque, "How Effective Are Existing Phosphorus Management Strategies in Mitigating Surface Water Quality Problems in the U.S," *Sustainability* 13 (2021): 6565, https://doi.org/10.3390/su13126565.

18. F. Solangi, X. Zhu, S. Khan, et al., "The Global Dilemma of Soil Legacy Phosphorus and Its Improvement Strategies Under Recent Changes in Agro-Ecosystem Sustainability," *ACS Omega* 8 (2023): 23271–23282, https://doi.org/10.1021/acsomega.3c00823.

19. Q. Ma, R. Bell, C. Scanlan, and A. Neuhaus, "Long-Term Rundown of Plant-Available Potassium in Western Australia Requires a Re-Evaluation of Potassium Management for Grain Production: A Review," *Crop Pasture Sci* 73 (2022): 981–996, https://doi.org/10.1071/CP21612.

20. E. Portela, F. Monteiro, M. Fonseca, and M. M. Abreu, "Effect of Soil Mineralogy on Potassium Fixation in Soils Developed on Different Parent Material," *Geoderma* 343 (2019): 226–234, https://doi.org/10.1016/j.geoderma.2019.02.040.

21. R. Borges, V. Prevot, C. Forano, and F. Wypych, "Design and Kinetic Study of Sustainable Potential Slow-Release Fertilizer Obtained by Mechanochemical Activation of Clay Minerals and Potassium Monohydrogen Phosphate," *Industrial & Engineering Chemistry Research* 56 (2017): 708–716, https://doi.org/10.1021/acs.iecr.6b04378.

22. Z. Zhang, C. Han, C. Tao, X. Fan, and R. Liu, "Preparation of Phosphogypsum–Bentonite-Based Slow-Release Potassium Magnesium Sulfate Fertilizer," *Agriculture (London)* 15 (2025): 692, https://doi.org/10.3390/agriculture15070692.

23. J. J. Weeks, Jr. and G. M. Hettiarachchi, "A Review of the Latest in Phosphorus Fertilizer Technology: Possibilities and Pragmatism," *Journal of Environmental Quality* 48 (2019): 1300–1313, https://doi.org/10.2134/jeq.2019.02.0067.

24. A. Khosravi, Y. Yuan, Q. Liu, et al., "Hydrochars as Slow-Release Phosphorus Fertilizers for Enhancing Corn and Soybean Growth in an Agricultural Soil," *Carbon Research* 3 (2024): 7, https://doi.org/10.1007/s44246-023-00086-w.

25. E. García-Ilizaliturri, E. Ibarra-Laclette, N. Pariona-Mendoza, et al., "Controlled-Release Phosphorus Fertilizers Manufactured With Chitosan Derivatives: An Effective Alternative for Enhanced Plant Development," *Plants* 14 (2025): 610, https://doi.org/10.3390/plants14040610.

26. X.-F. Tian, C.-L. Li, M. Zhang, Y.-Y. Lu, Y.-L. Guo, and L.-F. Liu, "Effects of Controlled-Release Potassium Fertilizer on Available Potassium, Photosynthetic Performance, and Yield of Cotton," *Journal of Plant Nutrition and Soil Science* 180 (2017): 505–515, https://doi.org/10.1002/jpln.201700005.

27. N. Herlina, S. N. H. Utami, M. Nurudin, and E. Hanudin, "Synthesis and Characterization of Slow Release Fertilizer Nitrogen and Slow Release Fertilizer Potassium Based on Biochar With Nanotechnology and Alginate," *Journal of Ecological Engineering* 26 (2025): 378–390, https://doi.org/10.12911/22998993/202978.

28. A. F. Santos, L. S. Mendes, P. Alvarenga, L. M. Gando-Ferreira, and M. J. Quina, "Nutrient Recovery via Struvite Precipitation From Wastewater Treatment Plants: Influence of Operating Parameters, Coexisting Ions, and Seeding," *Water* 16 (2024): 1675, https://doi.org/10.3390/w16121675.

29. I. Kabdaşlı, A. Siciliano, C. Limonti, and O. Tünay, "Is K-Struvite Precipitation a Plausible Nutrient Recovery Method From Potassium-Containing Wastes?—A Review," *Sustainability* 14 (2022): 11680, https://doi.org/10.3390/su141811680.

30. A. E.-E. A. Z. Amin, "Using Bone Char as a Renewable Resource of Phosphate Fertilizers in Sustainable Agriculture and Its Effects on Phosphorus Transformations and Remediation of Contaminated Soils as Well as the Growth of Plants," *Journal of Soil Science and Plant Nutrition - Springer Nature* 24 (2024): 6980–6998, https://doi.org/10.1007/s42729-024-02018-y.

31. J. Kruse, K. Panten, and N. Siebers, "The Fate of Phosphorus From Bone Char-Based Fertilizers in Soil Pools in a 5-Year Crop Rotation," *Nutrient Cycling in Agroecosystems* 124 (2022): 263–277, https://doi.org/10.1007/s10705-022-10228-y.

32. A. Demeyer, J. C. Voundi Nkana, and M. G. Verloo, "Characteristics of Wood Ash and Influence on Soil Properties and Nutrient Uptake: An Overview," *Bioresource Technology* 77 (2001): 287–295, https://doi.org/10.1016/S0960-8524(00)00043-2.

33. I. Maj, K. Niesporek, P. Płaza, J. Maier, and P. Łój, "Biomass Ash: A Review of Chemical Compositions and Management Trends," *Sustainability* 17 (2025): 4925, https://doi.org/10.3390/su17114925.

34. P. Luo, W. Zhang, D. Xiao, J. Hu, N. Li, and J. Yang, "Biochar-Based Fertilizers: Advancements, Applications, and Future Directions in Sustainable Agriculture—A Review," *Agronomy* 15 (2025): 1104, https://doi.org/10.3390/agronomy15051104.

35. S. Sharma, S. Mukherjee, S. Bolan, et al., "Biochar as a Potential Nutrient Carrier for Agricultural Applications," *Current Pollution Reports* 11 (2025): 19, https://doi.org/10.1007/s40726-025-00349-7.

36. S. Schwindenhammer and D. Gonglach, "Closing the Nutrient-Food Loop: Technology Innovation and (De)Politicization in European Nutrient Policy," *Frontiers in Political Science* 6 (2024): 1382338, https://doi.org/10.3389/fpos.2024.1382338.

37. A. M. Rashad, "Lightweight Expanded Clay Aggregate as a Building Material – An Overview," *Construction and Building Materials* 170 (2018): 757–775, https://doi.org/10.1016/j.conbuildmat.2018.03.009.

38. F. Andreola, A. Borghi, S. Pedrazzi, et al., "Spent Coffee Grounds in the Production of Lightweight Clay Ceramic Aggregates in View of Urban and Agricultural Sustainable Development," *Materials* 12 (2019): 3581, https://doi.org/10.3390/ma12213581.

39. D. Ronga, M. Parisi, L. Barbieri, I. Lancellotti, F. Andreola, and C. Bignami, "Valorization of Spent Coffee Grounds, Biochar and Other Residues to Produce Lightweight Clay Ceramic Aggregates Suitable for Nursery Grapevine Production," *Horticulturae* 6 (2020): 58, https://doi.org/10.3390/horticulturae6040058.

40. B. Ayati, V. Ferrándiz-Mas, D. Newport, and C. Cheeseman, "Use of Clay in the Manufacture of Lightweight Aggregate," *Construction and Building Materials* 162 (2018): 124–131, https://doi.org/10.1016/j.conbuildmat.2017.12.018.

41. F. G. A. Verheijen, A. Zhuravel, F. C. Silva, A. Amaro, M. Ben-Hur, and J. J. Keizer, "The Influence of Biochar Particle Size and Concentration on Bulk Density and Maximum Water Holding Capacity of Sandy vs Sandy Loam Soil in a Column Experiment," *Geoderma* 347 (2019): 194–202, https://doi.org/10.1016/j.geoderma.2019.03.044.

42. G. Allesina, N. M. Andreola, P. Tartarini, et al., Procedimento per utilizzare char da gassificazione e/o pirolisi con altri scarti industriali per la formulazione di materiali alleggeriti con effetto fertilizzante e di materiali polimerici per isolamento termico, 102018000009844, 2020, accessed October 29, 2025, https://iris.unimore.it/handle/11380/1237537.

43. Y. Gao, Z. Fang, L. Van Zwieten, et al., "A Critical Review of Biochar-Based Nitrogen Fertilizers and Their Effects on Crop Production and the Environment," *Biochar* 4 (2022): 36, https://doi.org/10.1007/s42773-022-00160-3.

44. J. Lu, Y. Li, Y. Cai, P. Jiang, and B. Yu, "Co-Incorporation of Hydrotalcite and Starch into Biochar-Based Fertilizers for the Synthesis of Slow-Release Fertilizers With Improved Water Retention," *Biochar* 5 (2023): 44, https://doi.org/10.1007/s42773-023-00242-w.

45. M. Khouloud, K. Ferji, J. Six, R. Beniazza, and M. Lahcini, "Clay-Based Modulation of Nutrient Release: Ghassoul as Nutrient Carrier for Enhanced Fertilizer Efficiency," *Emergent Materials* 8 (2025): 2883–2899, https://doi.org/10.1007/s42247-024-00943-3.

46. J. H. da Silva Soares, T. W. Boaventura, A. C. A. de Moura, et al., "Design and Performance of a Multicomponent Glass Fertilizer for Nutrient Delivery in Precision Agriculture," *ACS Agricultural Science & Technology* 5 (2025): 142–157, https://doi.org/10.1021/acsagscitech.4c00243.

47. A. Berezicka, J. Sułowska, and M. Szumera, "Alteration of Sulfur-Bearing Silicate-Phosphate (Agri)Glasses in Soil Environment: Structural Characterization and Chemical Reactivity of Fertilizer Glasses: Insights From 'In Vitro' Studies," *Molecules* 30 (2025): 1684, https://doi.org/10.3390/molecules30081684.

48. Y. Hu, J. Li, Y. Wu, D. Zhang, Z. Qi, and R. Yang, "Spent Coffee Ground and Its Derivatives as Soil Amendments—Impact on Soil Health and Plant Production," *Agronomy* 15, no. 2025): 26. https://doi.org/10.3390/agronomy15010026.

49. V. Topalović, A. Vujošević, A. Antanasković, et al., "Chemical Stability and Fertilizer Efficiency of Bioglass and Biochar on Rose Plantings," in *Proceedings of the XVI International Mineral Processing and Recycling Conference* (2025): 483–489, https://doi.org/10.5937/IMPRC25483T.

50. M. F. Barba, P. Callejas, J. O. Arzabe, and D. Ajò, "Characterization of Two Frit Ceramic Materials in Low Cost Fertilizers," *Journal of the European Ceramic Society* 18 (1998): 1313–1317, https://doi.org/10.1016/S0955-2219(98)00059-4.

51. F. Altimari, F. Andreola, I. Lancellotti, et al., "Effect of Using Rotational and Static Kilns on the Properties of Eco-Friendly Lightweight Aggregates Made With Pumice Scraps and Spent Coffee Grounds," *Materials* 18 (2025): 3692, https://doi.org/10.3390/ma18153692.

52. Ministero del lavoro, della salute e delle politiche sociali, commissione permanente per la revisione e la pubblicazione della farmacopea ufficiale, Saggi e procedimenti tecnologici, Capitolo 2.9, in: Farm. Uff. Della Repubblica Ital., XII (Istituto Poligrafico, Zecca dello Stato, 2008: pp. 366–367). 421–423.

53. Governo della Repubblica Italiana, Riordino e revisione della disciplina in materia di fertilizzanti, a norma dell'articolo 13 della legge 7 luglio 2009, n. 88, 2010. https://www.normattiva.it/atto/caricaDettaglioAtto?atto.dataPubblicazioneGazzetta=2010-05-26&atto.codiceRedazionale=010G009.

54. R. Betriani, S. Sutarno, I. Kartini, and J. Budiarta, "Synthesis of Zeolite/NPK Coated With Cu-Alginate-PVA-Glutaraldehyde as a Slow-Release Fertilizer," *Indonesian Journal of Chemistry* 23 (2023): 184–199, https://doi.org/10.22146/ijc.76205.

55. C. Vancea, G. Mosoarca, and S. Popa, "A Sustainable Solution to Obtain P-K-Mn Glass Fertilizers From Cheap and Readily Available Wastes," *International Journal of Environmental Research and Public Health* 18 (2021): 6585, https://doi.org/10.3390/ijerph18126585.

56. S. F. Valle, A. S. Giroto, V. Dombinov, A. A. Robles-Aguilar, N. D. Jablonowski, and C. Ribeiro, "Struvite-Based Composites for Slow-Release Fertilization: A Case Study in Sand," *Scientific Reports* 12 (2022): 14176, https://doi.org/10.1038/s41598-022-18214-8.

57. E. G. de Morais, K. Jindo, and C. A. Silva, "Biochar-Based Phosphate Fertilizers: Synthesis, Properties, Kinetics of P Release and Recommendation for Crops Grown in Oxisols," *Agronomy* 13 (2023): 326, https://doi.org/10.3390/agronomy13020326.

58. Quaderni IRSA-CNR n. 64., *Appendice II, Volume 3, Consiglio Nazionale delle Ricerche (CNR), Istituto di Ricerca sulle Acque* (IRSA, 1986).

59. Regulation (EU) 2019/1009 of the European Parliament and of the Council Laying Down Rules on the Making Available on the Market of EU Fertilising Products (European Parliament and Council of the European Union, 2022). https://eur-lex.europa.eu/eli/reg/2019/1009/2022-07-16/eng.

60. N. Lakshani, H. S. Wijerathne, C. Sandaruwan, N. Kottegoda, and V. Karunarathne, "Release Kinetic Models and Release Mechanisms of Controlled-Release and Slow-Release Fertilizers," *ACS Agricultural Science & Technology* 3 (2023): 939–956, https://doi.org/10.1021/acsagscitech.3c00152.

61. M. Chen, X. Wu, Y. Wang, et al., "$Ca(OH)_2$-Modified *Camellia oleifera* Shell Biochar: Preparation, Characterization, and Adsorption of NH_4^+ and PO_4^{3-}," *Biochar X* 2 (2026): e005, https://doi.org/10.48130/bchax-0026-0002.

62. K. Chen, L. Li, K. Yang, Q. Cao, and Y. Chen, "Efficient Adsorptive Removal of Potassium From Potassium Perrhenate Solution Using a Cationic Ion Exchange Resin," *RSC Advances* 15 (2025): 1604–1617, https://doi.org/10.1039/D4RA08404G.

63. S. H. H. A. Ali, M. Al-Qubaisi, M. Z. Hussein, M. Ismail, Z. Zainal, and M. N. Hakim, "Controlled Release and Angiotensin-Converting Enzyme Inhibition Properties of an Antihypertensive Drug Based on a Perindopril Erbumine-Layered Double Hydroxide Nanocomposite," *International Journal of Nanomedicine* 7 (2012): 2129–2141, https://doi.org/10.2147/IJN.S30461.

64. M. Meena, D. Jegadeeswari, B. K. Sathiya, R. Rajeswari, A. Senthil, and K. Boomiraj, "Aqueous Release Kinetics of Nitrogen and Potassium From a Citric Acid–Crosslinked Lignosulfonate Biopolymer Matrix," *Plant Science Today* 13 (2026): 1–9, https://doi.org/10.14719/pst.14444.

65. W. Zhu, J. Long, and M. Shi, "Release Kinetics Model Fitting of Drugs With Different Structures From Viscose Fabric," *Materials* 16 (2023): 3282, https://doi.org/10.3390/ma16083282.

66. A. D'Angelo, V. Viola, M. Fiorentino, G. Dal Poggetto, and I. Blanco, "Use of Natural Dyes to Color Metakaolin-Based Geopolymer Materials," *Ceramics International* 51 (2025): 5528–5535, https://doi.org/10.1016/j.ceramint.2024.05.109.

67. G. R. Regione Lombardia. Linee guida relative alla costruzione e all'esercizio degli impianti di produzione di compost – Revoca della D.G.R. 16 luglio 1999, n. 0 (2003): 44263. https://www.isprambiente.gov.it/it/progetti/cartella-progetti-in-corso/suolo-e-territorio-1/uso-dei-fanghi-di-depurazione-in-agricoltura-attivita-di-controllo-e-vigilanza-del-territorio/files/LOMBARDIA_DGR_12764_2003_Linee_guida_Compostaggio.pdf.

68. R. L. Carr, "Evaluating Flow Properties of Solids," *Chemical Engineering* 72 (1965): 163–168.

69. K. G. Karapetyan, V. A. Senichenkov, G. S. Zenin, and M. N. Ryabova, "Kinetics of Dissolution of Glassy Fertilizers," *Russian Journal of Applied Chemistry* 78 (2005): 1383–1385, https://doi.org/10.1007/s11167-005-0522-6.

70. J. Yliniemi, "Surface Layer Alteration of Multi-Oxide Silicate Glasses at a Near-Neutral pH in the Presence of Citric and Tartaric Acid," *Langmuir: The ACS Journal of Surfaces and Colloids* 38 (2022): 987–1000, https://doi.org/10.1021/acs.langmuir.1c02378.

71. M. Javan, A. Abtahi, G. Zareian, and H. Haghighatnia, "Soil Mineralogy and Potassium Forms Distribution and Release in Some Calcareous Soils of the Darab Region, Iran," *PLoS One* 20 (2025): e0334155, https://doi.org/10.1371/journal.pone.0334155.

72. L. Brečević and H. Füredi-Milhofer, "Precipitation of Calcium Phosphates From Electrolyte Solutions," *Calcified Tissue Research* 10 (1972): 82–90, https://doi.org/10.1007/BF02012538.

73. E. Książek, "Citric Acid: Properties, Microbial Production, and Applications in Industries," *Molecules* 29 (2023): 22, https://doi.org/10.3390/molecules29010022.

74. C. Righi, F. Barbieri, E. Sgarbi, et al., "Suitability of Porous Inorganic Materials From Industrial Residues and Bioproducts for Use in Horticulture: A Multidisciplinary Approach," *Applied Sciences* 12 (2022): 5437. https://doi.org/10.3390/app12115437.

75. L. B. Williams, D. W. Metge, D. D. Eberl, et al., "What Makes a Natural Clay Antibacterial?," *Environmental Science and Technology* 45 (2011): 3768–3773, https://doi.org/10.1021/es1040688.

76. L. B. Williams and S. E. Haydel, "Evaluation of the Medicinal Use of Clay Minerals as Antibacterial Agents," *International Geology Review* 52 (2010): 745–770, https://doi.org/10.1080/00206811003679737.

77. G. C. Díaz-Hernández, P. Alvarez-Fitz, Y. I. Maldonado-Astudillo, et al., "Antibacterial, Antiradical and Antiproliferative Potential of

Green, Roasted, and Spent Coffee Extracts," *Applied Sciences* 12 (2022): 1938, https://doi.org/10.3390/app12041938.

78. A. Nonthakaew, Na. Matan, T. Aewsiri, and Ni. Matan, "Caffeine in Foods and Its Antimicrobial Activity," *International Food Research Journal* 22, no. 1 (2015): 9–14, http://www.ifrj.upm.edu.my/22(01)2015/(2).pdf.

79. I. H. Ifijen, E. Faderin, C. E. Okafor, et al., "Dual Functionality of Cobalt Oxide Nanoparticles: Exploring Their Potential as Antimicrobial and Anticancer Agents," *Biomedical Materials & Devices* 4 (2026): 143–188, https://doi.org/10.1007/s44174-025-00276-7.

Supporting Information

Additional supporting information can be found online in the Supporting Information section.
Supporting File: appl70173-sup-0001-Figure_S1.jpg.